ADVANCED OPTICAL MATERIALS
www.advopticalmat.de

Advancements in Halide Perovskite Large Single Crystal Photodetectors: Bridging Optical and Ionizing Radiation

Zhengxun Lai, Yi Shen, He Shao, You Meng, and Johnny C. Ho**

Halide perovskite large single crystals (HPLSCs, with millimeter-scale dimensions) are promising materials for photodetection, effectively bridging optical and ionizing radiation regimes with superior optoelectronic properties. This review explores recent advancements in HPLSC-based photodetectors, emphasizing synthesis methods, device architectures, and performance enhancements. Techniques like temperature-lowering crystallization, inverse-temperature crystallization, and antisolvent vapor-assisted crystallization produce high-quality HPLSCs with minimal defects, extended carrier diffusion, and improved storage stability. These crystals excel across spectral domains: visible detectors achieve responsivities over 100 A W^{-1}, UV devices offer microsecond response speeds, and infrared detectors utilize defect engineering for broadband sensitivity. In ionizing radiation detection, HPLSCs perform well due to high atomic number constituents and substantial thickness, yielding X-ray sensitivities above 10^5 μC Gy$_{air}$$^{-1}$ cm^{-2} and γ-ray energy resolutions comparable to commercial detectors. Lead-free alternatives address toxicity concerns while maintaining efficacy. Future research is expected to focus on hybrid growth techniques, AI-driven material discovery, and integrated multispectral imaging, highlighting HPLSCs' potential in medical imaging, environmental monitoring, and aerospace applications.

1. Introduction

Photodetectors are vital components across diverse technological sectors, precisely converting optical signals into electrical outputs. Their performance impacts systems in medical imaging, industrial inspection, and consumer electronics by influencing resolution, dynamic range, and response time.[1–3] In fiber-optic communications, they facilitate terabit-scale data transmission, while emerging 5G/6G networks and quantum communication systems demand ultrabroad spectral response and sub-nanosecond response times.[4,5] Environmental monitoring requires UV-to-IR detectors capable of real-time analysis of pollutants, necessitating spectral versatility and environmental stability under varying conditions.[6] These applications drive the development of next-generation photodetectors optimized for sensitivity, noise, spectral coverage, cost-efficiency, and environmental robustness.

Halide perovskites represent a revolutionary semiconductor class in optoelectronics, offering high absorption coefficients, tunable bandgaps, long carrier diffusion lengths, and notable defect tolerance.[7–9] Perovskite light-emitting diodes boast narrow emission linewidths and quantum efficiencies exceeding 30%,[10,11] while photovoltaic devices achieve power conversion efficiencies over 26%, rivaling silicon.[12,13] Rapid advances in perovskite photodetectors have enabled broad spectral responses from γ-ray to near-infrared (NIR).[14–19] Moreover, their ultralow production costs further enhance practical value, particularly for high-replacement applications, such as radioprotection dosimeters and medical diagnostic detectors.

The term "perovskite" originates from the mineral calcium titanate ($CaTiO_3$), with halide perovskites adopting a similar structure, substituting oxygen with halides, forming ABX_3 compounds. A represents monovalent cations, including alkali metals (e.g., Cs^+, Rb^+) or organic cations (e.g., methylammonium MA^+, formamidinium FA^+). B denotes divalent metals, such as Pb^{2+} or Sn^{2+}. X includes halide anions (I^-, Br^-, Cl^-). In the ABX_3 structure, each B-site cation is octahedrally coordinated by six X^- anions, forming $[BX_6]$ octahedra. These octahedra interconnect via corner-sharing to create a 3D network, while A-site cations occupy the interstitial spaces (**Figure 1a**). This architecture endows the material with exceptional carrier transport properties and tunable optical bandgaps.

Z. Lai, Y. Meng
Changsha Semiconductor Technology and Application Innovation Research Institute
College of Semiconductors (College of Integrated Circuits)
Hunan University
Changsha 410082, China
E-mail: youmeng@hnu.edu.cn

Y. Shen, H. Shao, J. C. Ho
Department of Materials Science and Engineering
City University of Hong Kong
Kowloon, Hong Kong SAR 999077, China
E-mail: johnnyho@cityu.edu.hk

J. C. Ho
State Key Laboratory of Terahertz and Millimeter Waves
City University of Hong Kong
Kowloon, Hong Kong SAR 999077, China

J. C. Ho
Shenzhen Research Institute
City University of Hong Kong
Shenzhen 518057, China

J. C. Ho
Institute for Materials Chemistry and Engineering
Kyushu University
Fukuoka 816-8580, Japan

The ORCID identification number(s) for the author(s) of this article can be found under https://doi.org/10.1002/adom.202501562

DOI: 10.1002/adom.202501562

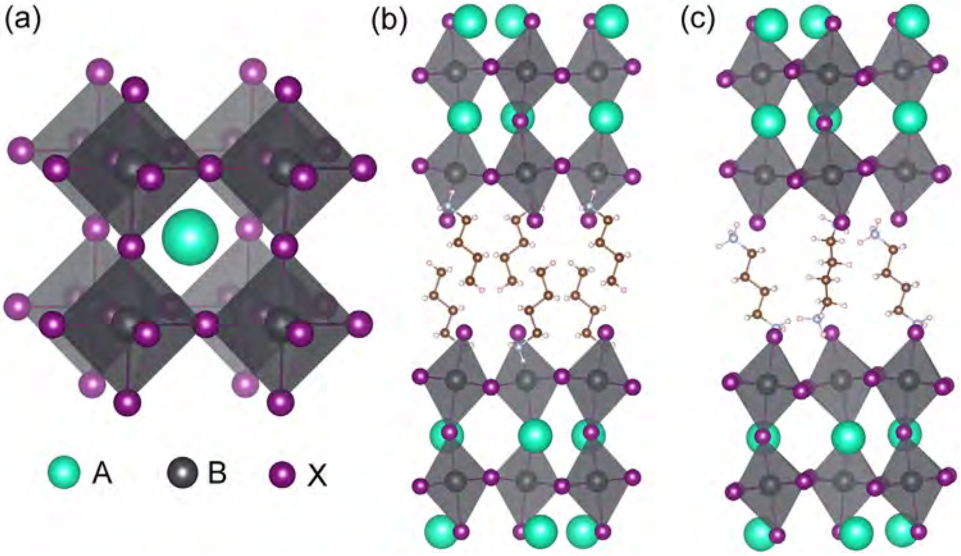

Figure 1. Schematic of the crystal structures of a) 3D, b) quasi-2D Ruddlesden–Popper type and c) quasi-2D Dion–Jacobson type halide perovskites.

However, conventional 3D perovskites easily degrade under ambient conditions, such as moisture, heat, and electron beam stress.[20] To address these limitations, researchers introduced bulkier organic cations (denoted as A' or A'') into the structure, leading to the development of 2D perovskites with the general formula $(A')_2(A)_{n-1}B_nX_{3n+1}$ for Ruddlesden–Popper type and $A''(A)_{n-1}B_nX_{3n+1}$ for Dion–Jacobson (DJ) type. The voluminous A' or A" cations cannot fit into the interstices of the 3D framework, forcing the $[BX_6]$ octahedral network to split into layered 2D sheets. These layers are stacked via van der Waals interactions or hydrogen bonds mediated by the A′ (or A″) cations (Figure 1b,c). The layer thickness, defined by the n-value (number of octahedral layers per slab), governs the quantum confinement effect: smaller n values result in larger bandgaps (blueshift) and reduced carrier mobility. Compared to their 3D counterparts, 2D perovskites exhibit enhanced environmental stability, tunable optoelectronic properties, and lower defect densities due to the protective organic spacer layers. Furthermore, the perovskite family has also extended to derivative structures, such as $A_3B_2X_9$ (e.g., $Cs_3Bi_2I_9$).[21] While retaining the A-site cations and X-site halides of classical perovskites, these derivatives feature trivalent B-site metals (e.g., Bi^{3+}, Sb^{3+}) instead of divalent Pb^{2+}. This substitution reduces toxicity by eliminating lead and leverages the high atomic number (Z) of B-site elements for enhanced X-ray attenuation, making $A_3B_2X_9$ materials particularly promising for radiation detection applications.[22,23]

Currently, most perovskite optoelectronic devices, such as solar cells and light-emitting transistors, employ polycrystalline thin films due to limitations in device characteristics and fabrication methodologies. In contrast, halide perovskite large single crystals (HPLSCs, with millimeter-scale dimensions) exhibit superior optoelectronic properties, including enhanced structural integrity, reduced defect density, elevated carrier mobility, accelerated charge transport, extended carrier diffusion lengths, heightened absorption coefficients, suppressed ion migration, and improved moisture resistance and thermal stability. It nees to be pointed out that advanced thin-film technologies have recently achieved comparable stability through defect passivation and interface engineering.[24–26] These attributes are particularly advantageous for photodetector applications, where superior light absorption and rapid carrier transport in bulk single crystals significantly enhance device performance. For ionizing radiation detection, HPLSCs are uniquely suited due to their capacity to absorb high-penetration-depth radiation effectively. The large crystal dimensions enable efficient energy absorption, thereby boosting detector sensitivity and signal-to-noise ratios.

In this review, we systematically examine recent advancements in HPLSC-based photodetectors. The discussion begins with an overview of synthesis strategies for HPLSCs, followed by a critical evaluation of their applications in optical and ionizing radiation detection. We categorize these photodetectors based on operational wavelength regimes (from γ-ray to NIR) and focus on innovations in material synthesis, device architecture design, and performance enhancement mechanisms. Additionally, we highlight emerging application scenarios enabled by HPLSC photodetectors. Finally, we critically assess persistent challenges and propose future research directions to advance this field toward industrial adoption.

2. The Growth Methods of HPLSCs

Various methodologies have been developed for synthesizing high-quality HPLSCs, including temperature-lowering crystallization (TLC), inverse-temperature crystallization (ITC), slow solvent evaporation method (SSE), and antisolvent vapor-assisted crystallization (AVC). These techniques share a common principle: inducing a supersaturated state in perovskite precursor solutions to drive nucleation and subsequent crystal growth. Building upon these foundational approaches, researchers have developed advanced modifications to enhance control over nucleation and growth kinetics. For instance, seeding techniques, such as top-seeded solution growth (TSSG) and bottom-seeded solution growth (BSSG), have been introduced, where pre-existing seed crystals guide oriented nucleation, minimizing random defect

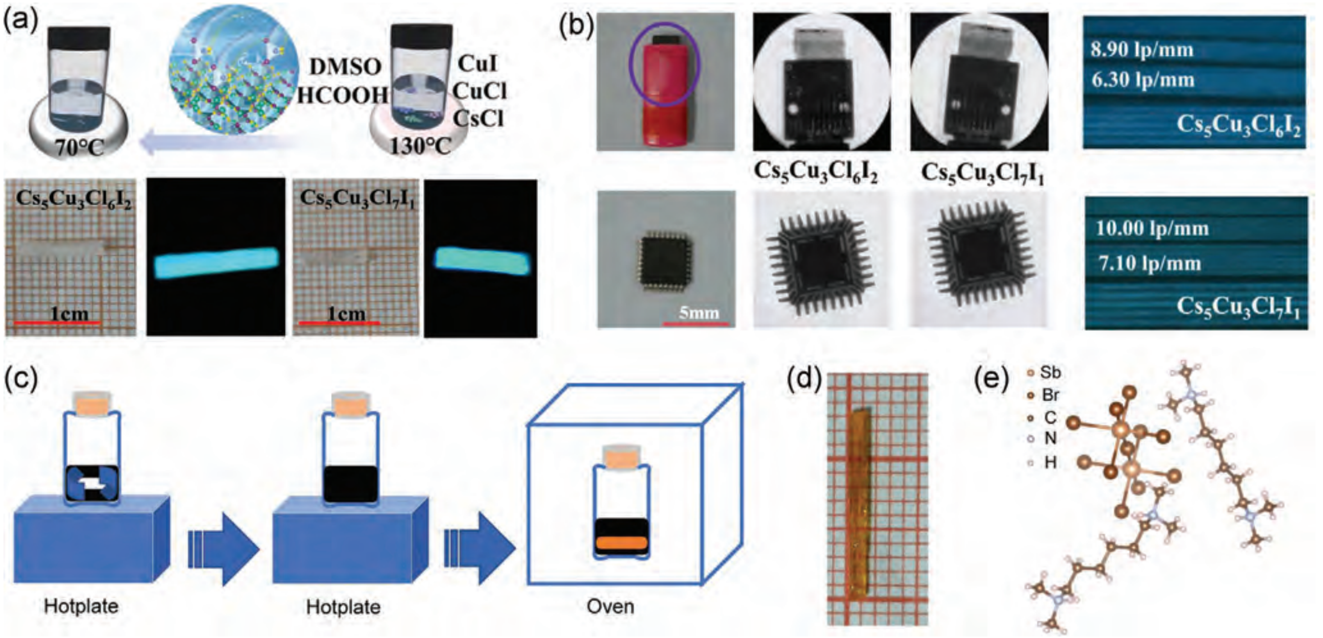

Figure 2. a) The demonstration of the fabrication process of $Cs_5Cu_3Cl_6I_2$ and $Cs_5Cu_3Cl_7I_1$ HPLSCs via the TLC method, and their photographs with and without a 302-nm-UV-lamp illumination. b) The X-ray images of a chip, a card, and the spatial resolution measurement result.[27] Copyright 2025, Elsevier. c) Procedure for crystal growth of the (TMHD)$SbBr_5$ HPLSCs. d) Photograph of a (TMHD)$SbBr_5$ HPLSC. e) The asymmetric unit of (TMHD)$SbBr_5$.[28] Copyright 2024, John Wiley and Sons.

formation. Beyond the solution-based methods discussed above, the Bridgman technique offers a robust alternative for synthesizing single crystals of less-soluble perovskites. In recent years, many innovative strategies have expanded the toolkit for perovskite crystal growth. Herein, we provide a detailed examination of these techniques.

2.1. Temperature-Lowering Crystallization (TLC)

TLC is a solution-based technique for growing high-quality HPLSCs by gradually decreasing the temperature of a precursor solution to induce supersaturation and controlled nucleation. TLC exploits the positive temperature-solubility relationship of perovskite precursors in solvents (e.g., dimethylformamide (DMF), γ-butyrolactone (GBL), and halogen acid). This method is particularly advantageous for producing large, low-defect crystals with tailored optoelectronic properties. Below, we detail its principles, methodologies, and recent advancements. The TLC process hinges on the gradual reduction of solubility as the solution cools. Key steps include: At temperatures above the saturation point (80–100 °C, exceeding the crystallization threshold of the perovskite), perovskite precursors (e.g., PbI_2 and MAI for $MAPbI_3$) fully dissolve to form a homogeneous solution. Then, the solution is cooled at a defined rate (e.g., 1–3 $°C\ h^{-1}$), reducing solubility and driving the system into a supersaturated state. Nucleation initiates at critical supersaturation, followed by layer-by-layer crystal growth under kinetic control. For the TLC method, the cooling rate directly impacts crystal quality: slower rates (e.g., 1 $°C\ h^{-1}$) minimize thermal stress and defects, yielding larger, more uniform crystals.

Lin et al. synthesized high-quality quasi-1D $Cs_5Cu_3Cl_6I_2$ and $Cs_5Cu_3Cl_7I_1$ HPLSCs by the TLC method (**Figure** 2a). By strategically substituting chloride ions (Cl^-) with iodide ions (I^-), they engineered novel low-dimensional copper-based halide crystals that simultaneously mitigate the instability of conventional copper halides (e.g., $Cs_3Cu_2Cl_5$) under ambient conditions and retain exceptional luminescent properties. Leveraging these crystals as scintillators, the team achieved high-resolution X-ray imaging with spatial resolution down to 13.9 lp mm^{-1} (Figure 2b). This work addresses the longstanding challenge of scalable synthesis for copper halides, demonstrating TLC's capability to produce phase-pure, millimeter-sized crystals—a critical advancement for industrial applications.[27]

Some new types of HPLSCs have also been obtained through this method. Tang et al. synthesized a novel 1D perovskite-like (TMHD)$SbBr_5$ HPLSC for high-performance direct X-ray detection via the TLC method (Figures 2c,d). To acquire large crystals of high quality, seed crystals were introduced into the solution during the TLC temperature-controlled cooling process. The material's 1D chain structure of $SbBr_6$ octahedra is linked via van der Waals forces and hydrogen bonds (Figure 2e). The unique anisotropic carrier transport due to aligned $SbBr_6$ octahedral chains enabled directional charge collection and anisotropic X-ray response.[28]

2.2. Inverse-Temperature Crystallization (ITC)

Unlike the TLC method, where solubility decreases with cooling, ITC exploits the unique thermodynamic property of certain solvents in which the solubility of perovskite precursors decreases with increasing temperatures. This counterintuitive behavior enables rapid and controllable crystallization at elevated temperatures. The ITC mechanism hinges on the non-monotonic solubility-temperature relationship of perovskite precursors in specific polar solvents, such as GBL, DMF, or dimethyl sulfoxide (DMSO). The process involves: at room temperature, perovskite precursors (the corresponding halide constituents of the perovskite) fully dissolve in the solvent, forming a transparent precursor solution. Then, the solution is heated to more than 100 °C, and the solubility of the precursors decreases sharply, driving the system into a supersaturated state. At this stage, spontaneous nucleation occurs, followed by gradual crystal growth under controlled temperature conditions. The process is governed by the Gibbs free energy balance between dissolution and crystallization, where heating shifts the equilibrium toward crystal formation.

Liu et al. investigated the role of Cs^+ incorporation in $MAPbI_3$ HPLSCs. By partially substituting organic MA^+ ions with inorganic Cs^+ ions, they synthesized $MA_{1-x}Cs_xPbI_3$ HPLSCs by the ITC method (**Figure** 3a). γ-valerolactone was introduced as a novel solvent to replace the commonly used GBL, which faced policy restrictions, ensuring compliance with regulatory requirements. They found that the Cs^+ incorporation induced lattice contraction, suppressed defect formation, inhibited ion migration, and enhanced carrier mobility. The optimized $MA_{0.96}Cs_{0.04}PbI_3$ HPLSC exhibited exceptional X-ray detection performance compared with the $MAPbI_3$ without Cs (Figure 3b).[29]

Jin et al. synthesized $MAPbBr_3$ HPLSCs using the ITC method (Figure 3c). In this work, the coexistence of both electron- and hole-polarons in $MAPbBr_3$ was experimentally resolved within the initial 5 ps after photoexcitation for the first time. This was achieved using optical-pump THz-probe spectroscopy combined with the Drude–Smith–Lorentz model. They also found that polarons in HPLSCs exhibited much longer lifetimes (>300 ps) than films (≈5 ps) due to reduced grain-boundary scattering and lower trap density. Leveraging the high-quality $MAPbBr_3$ HPLSCs synthesized via the ITC method, this work establishes a robust experimental platform for directly investigating and controlling polaron dynamics in perovskite systems.[30]

2.3. Slow Solvent Evaporation Method (SSE)

The SSE method is a versatile and widely used technique for synthesizing HPLSCs. Leveraging controlled solvent removal under ambient or regulated conditions enables the growth of large, low-defect crystals with tailored optoelectronic properties. The slow solvent evaporation relies on gradual solvent removal to induce supersaturation and subsequent crystallization. Perovskite precursors are dissolved in a polar solvent (e.g., DMF, DMSO, or GBL) at room or elevated temperatures. As the solvent evaporates slowly, the solution becomes supersaturated, triggering nucleation. Eventually, nuclei grow gradually under kinetic control, minimizing defects and strain. The quality of the HPLSCs synthesized by the SSE method is governed by the evaporation rate, type of solvent, temperature, and humidity during the crystal growth.

Wang et al. reported the design and synthesis of two organic–inorganic hybrid HPLSCs, $(C_4H_{10}NO)PbX_3$ (X = Cl, Br), through the SSE method (**Figure** 4a). They found that due to the large radius of iodide ions and the instability of iodide, the I-based HPLSCs with high-quality growth are difficult. During the crystal growth process, the reagent bottle containing the precursor was covered with perforated foil to regulate the volatilization rate and reduce the amount of nucleation. By replacing a carbon atom in piperidine with an electronegative oxygen, morpholine (C_4H_8NO) was introduced as an organic cation. This substitution induced significant distortions in the inorganic $[PbX_6]$ octahedra, breaking structural symmetry and yielding non-centrosymmetric orthorhombic crystals (Figure 4b).[31]

The SSE method has also enabled the synthesis of novel HPLSCs. Abdi et al. used this method to synthesize a new halide perovskite, $C_2H_5NH_3BaCl_3$. During the evaporation of the solvent, the precursor was kept at room temperature and was contained in a low-diameter container (small surface). They found that if beakers or crystallizers with a larger surface were used, the crystallization rate would increase, and the quality of the HPLSCs would be worse. By controlling the evaporation rate, for the first time, they synthesized lead-free $C_2H_5NH_3BaCl_3$ HPLSCs by the SSE method.[33]

Luo et al. synthesized a lead-free bismuth halide perovskite ferroelectric HPLSC $[H_2mdap]BiBr_5$ (H_2mdap = N-methyl-1,3-diaminopropanium) by the SSE method (Figures 4c,d). They replaced toxic lead with environmentally friendly bismuth, addressing safety concerns in medical and environmental applications. Leveraging its ferroelectric-photovoltaic (FE-PV) effect driven by intrinsic spontaneous polarization, the material achieved zero-bias X-ray detection without external power (Figure 4e,f).[32]

2.4. Antisolvent Vapor-Assisted Crystallization (AVC)

Anti-solvents are widely used and crucial in the preparation of perovskite films.[36] The AVC method is also widely employed to grow high-quality halide perovskite single crystals (HPSCs). This method leverages the controlled introduction of antisolvent vapors to induce supersaturation and regulate nucleation kinetics, enabling the synthesis of large, low-defect crystals. AVC operates on the principle of solubility reduction triggered by antisolvent diffusion into the perovskite precursor solution. Key steps include: Precursor Dissolution: Perovskite precursors are dissolved in a polar solvent (e.g., DMF, DMSO) to form a homogeneous solution. The solution is exposed to antisolvent vapors (e.g., chloroform, toluene), which are miscible with the host solvent but reduce the solubility of perovskite precursors. This induces localized supersaturation, promoting nucleation. Nuclei grow into single crystals under optimized vapor pressure and temperature conditions, minimizing defects and ensuring uniformity. The process avoids thermal gradients and convective turbulence, common issues in temperature-dependent methods like ITC and AVC.

The AVC method has been continuously optimized since its initial proposal. Xu et al. investigated the critical role of hypophosphorous acid (H_3PO_2) in the growth of high-quality $Cs_3Cu_2I_5$ HPLSCs via the AVC method; the schematic illustration of procedures is shown in **Figure** 5a. They found that by

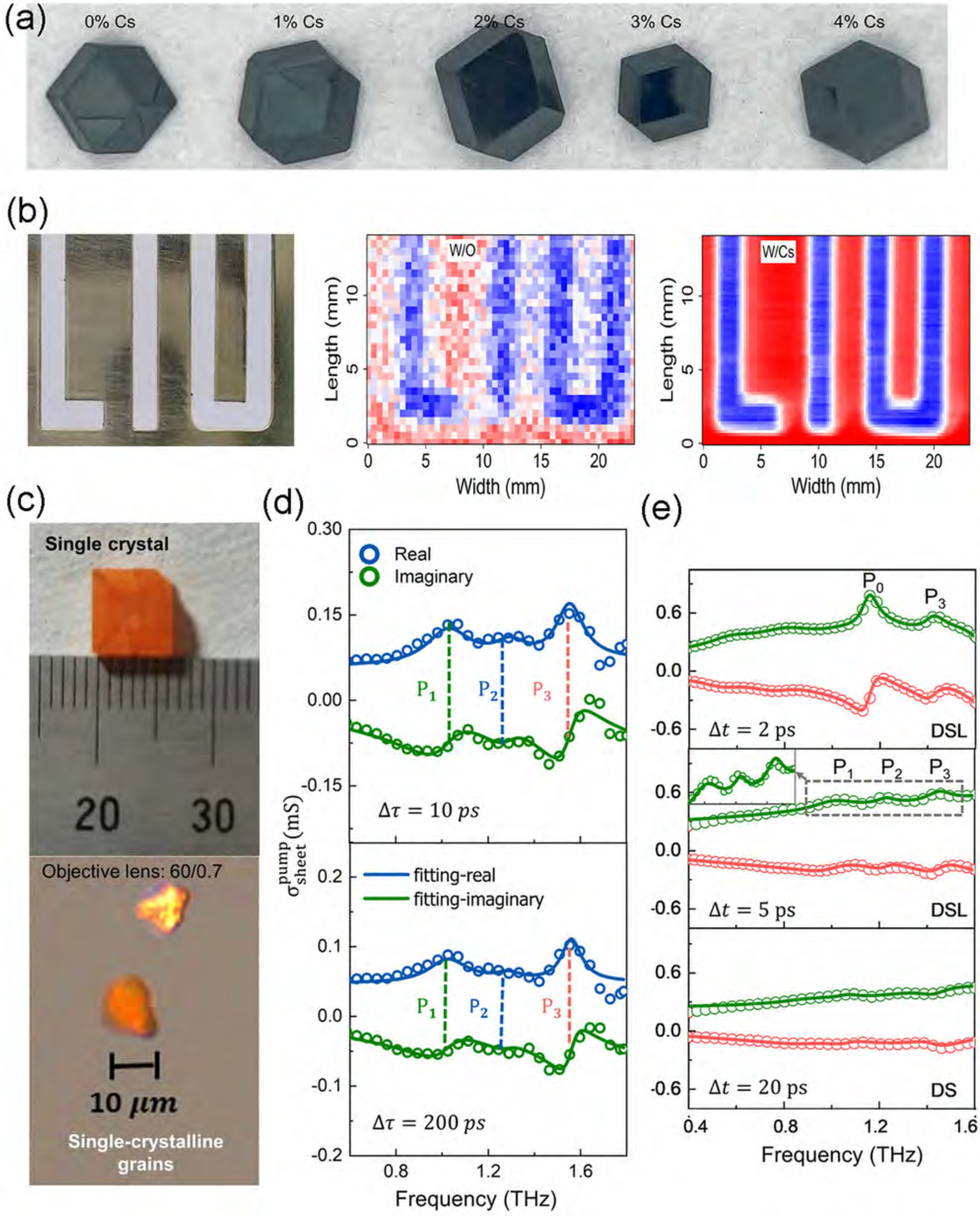

Figure 3. a) Photographs of the $MA_{1-x}Cs_xPbI_3$ HPLSCs (x = 0-0.04). b) Photograph of the object used for imaging measurements and the corresponding X-ray image measured by the $MAPbI_3$ HPLSC and the $MA_{0.96}Cs_{0.04}PbI_3$ HPLSC detectors, respectively.[29] Copyright 2025, John Wiley and Sons. c) Optical microscopy of $MAPbBr_3$ HPLSC and single-crystalline grain sample. Real and imaginary parts of the sheet photoconductivity spectra of $MAPbBr_3$ d) HPLSCs and e) films.[30] Copyright 2025, American Chemical Society.

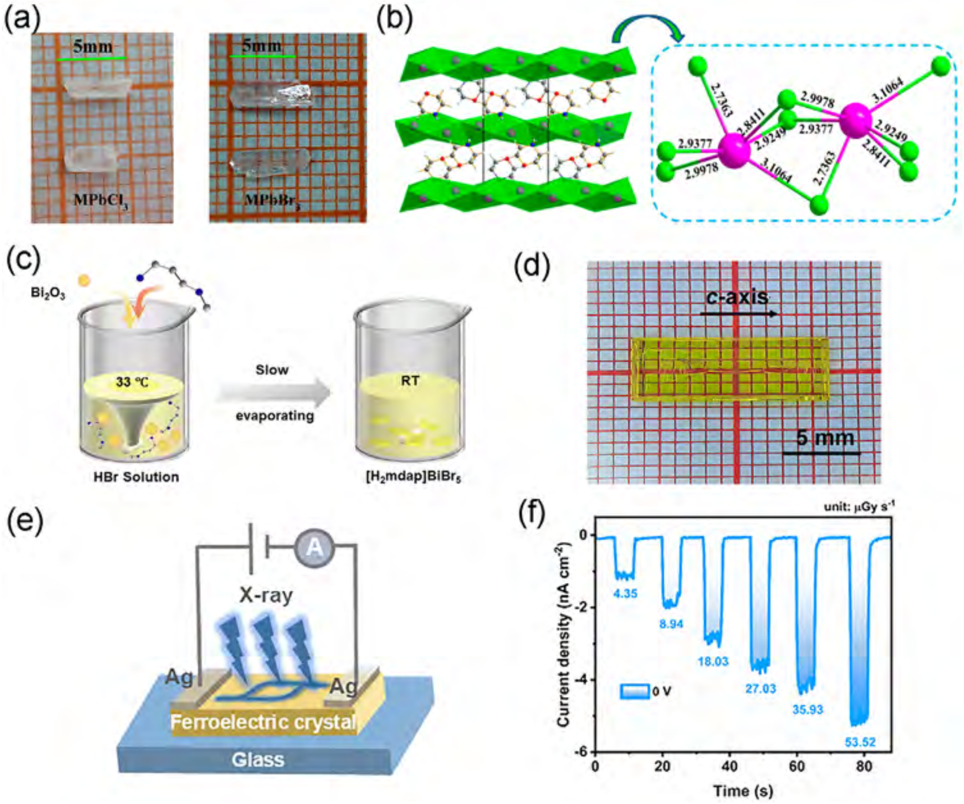

Figure 4. a) Photographs of as-grown $(C_4H_{10}NO)PbCl_3$ and $(C_4H_{10}NO)PbBr_3$ HPLSCs. b) Crystal structure and face-sharing distorted $PbCl_6$ octahedrons of $(C_4H_{10}NO)PbCl_3$.[31] Copyright 2025, American Chemical Society. c) Schematic for the growth of the $[H_2mdap]BiBr_5$ HPLSC. d) A photograph for the $[H_2mdap]BiBr_5$ HPLSC. e) The device schematic of the X-ray detector. f) Photoresponses of the $[H_2mdap]BiBr_5$ detector to X-rays at increased dose rates at 0 V bias.[32] Copyright 2025, Royal Society of Chemistry.

increasing solution acidity, H_3PO_2 dissolves precursor colloids and improves halide solubility in DMF. This synergy enables rapid growth of centimeter-sized $Cs_3Cu_2I_5$ crystals with well-defined crystallographic planes and minimal defects (Figure 5b). H_3PO_2 in the solution can reduce oxidized species (Cu^{2+}, I_2, I_3^-) to Cu^+ and I^-, stabilizing the precursor solution. Besides, the enhanced acidity can also promote the dissolution of CsI/CuI colloids, increasing ion availability and accelerating crystal growth. The elucidated role of H_3PO_2 in the AVC method in this work opens avenues for optimizing the growth of HPLSCs.[34]

Recently, the crystal growth dynamics of AVC have been precisely captured. Cheng et al. developed an imaging system with a 2-min sampling interval to track crystal growth dynamics in the AVC method. A custom image recognition algorithm quantified crystal size evolution, enabling precise measurement of growth rates (Figure 5c,d). This addressed previous limitations of long sampling intervals and inaccuracies in growth rate determination. They then demonstrated that regulating antisolvent vapor flux directs nucleation to the container-solution interface, yielding double-sided smooth crystals (Figure 5e). This minimized surface defects and reduced post-growth polishing requirements, critical for high-energy radiation detection applications. This work achieved the integration of real-time monitoring, kinetic modeling, and parameter optimization in AVC, enabling the reproducible synthesis of ultrahigh-quality PSCs.[35]

2.5. Bridgman Method

The Bridgman method is a classical crystal growth technique traditionally used for melt-grown crystals, but modified versions have been adapted for solution-based growth of HPLSCs. This method leverages precise temperature gradients and controlled solidification to produce large, high-quality crystals with minimal defects. The Bridgman method involves directional solidification of a molten precursor within a temperature gradient. Key steps of the Bridgman method include: A stoichiometric mixture of perovskite precursors (e.g., PbI_2 and CsI for $CsPbI_3$) is loaded into a sealed ampoule or crucible. The crucible is then placed in a furnace with a vertical temperature gradient, where the top zone is heated above the precursor's melting or dissolution temperature, and the bottom zone is cooled. The crucible is slowly lowered through the gradient, inducing crystallization from the bottom upward. The Bridgman method can achieve ultrahigh crystallinity and cm-scale crystal dimensions through controlled directional solidification, eliminating solvent contamination.

$CsPbBr_3$, a promising room-temperature γ-ray detector material, suffers from phase transitions (cubic → tetragonal → orthorhombic) during cooling, causing cracking and twin domains in Bridgman-grown crystals. To solve this problem, Klepov et al. synthesized $Cs(Pb_{0.75}Sn_{0.25})(Br_1Cl_2)$ HPLSCs by the Bridgman method (**Figure** 6a), yielding crack-free crystals in 1 week, significantly faster than traditional $CsPbBr_3$ growth

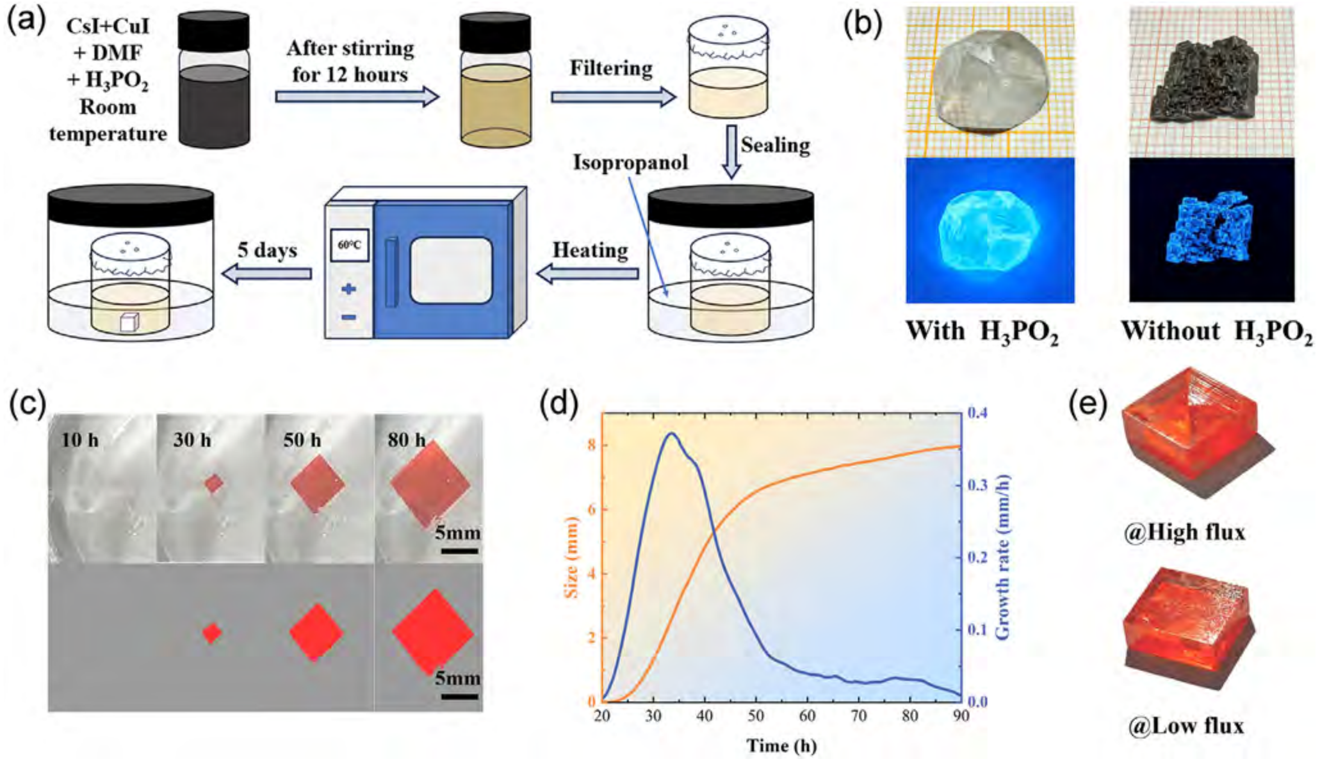

Figure 5. a) Schematic illustration of the AVC procedures with the addition of H_3PO_2. b) Photograph of the $Cs_3Cu_2I_5$ HPLSCs grown with and without H_3PO_2. Upper: under natural light; lower: under 302 nm UV light irradiation.[34] Copyright 2024, Elsevier. Measurement of $MAPbBr_3$ HPLSC growth rate: c) Pixelation processing of the raw images. d) Variation of crystal size and growth rate over time. e) Single crystals under different antisolvent vapor fluxes.[35] Copyright 2025, Elsevier.

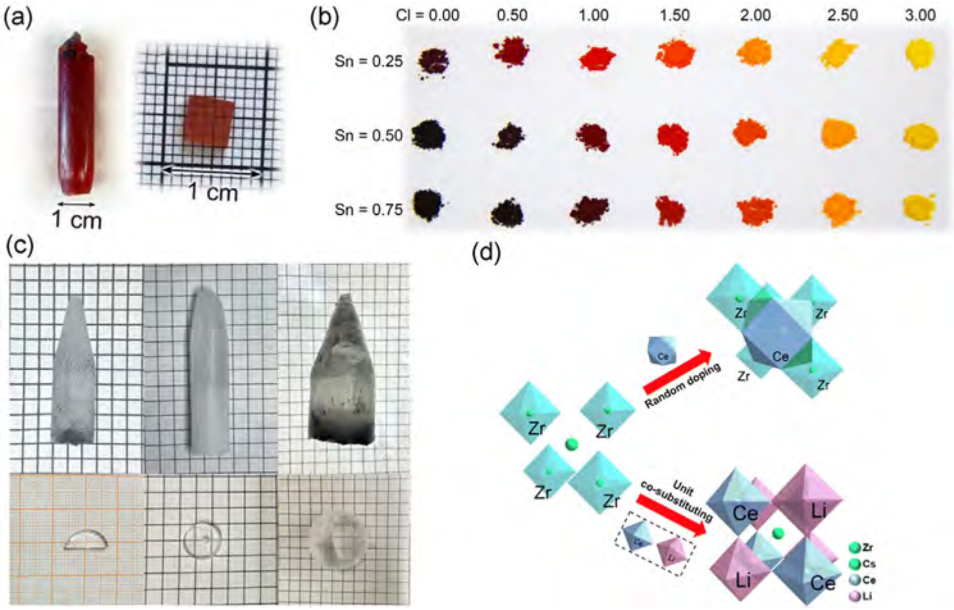

Figure 6. a) Bridgman growth of a $Cs(Pb_{0.75}Sn_{0.25})(Br_{1.00}Cl_{2.00})$ ingot and a polished crystal from a cleaved part of the ingot. b) Optical properties of $Cs(Pb_{1-x}Sn_x)(Br_{3-y}Cl_y)$ solid solutions.[37] Copyright 2024, Springer Nature. c) As-grown CZC, CZC:0.5%Ce, and CZC:20%(Ce, Li) HPLSCs. d) Schematic diagram of doping strategy.[38] Copyright 2025, Royal Society of Chemistry.

(≈3 weeks). In the HPLSCs, Sn^{2+} replaced Pb^{2+} (smaller ionic radius), and Cl^- replaced Br^- (smaller anion) (Figure 6b), adjusting the Goldschmidt tolerance factor to favor cubic symmetry. This work provides a strategy to overcome the intrinsic limitations of $CsPbBr_3$ HPLSCs by leveraging Sn/Cl co-substitution to stabilize cubic-phase perovskites through the Bridgman method.[37]

Wang et al. grew three types of HPLSCs via the Bridgman method: pure Cs_2ZrCl_6 (CZC), randomly doped CZC:0.5%Ce, and unit co-substituted CZC:20%(Ce, Li). The co-substitution strategy involved replacing Zr^{4+} with Ce^{3+} and adjacent vacancies with Li^+(Figure 6c), forming a stable ordered double perovskite structure ($Cs_2Zr_{1-x}(Ce, Li)_xCl_6$). They found that the unit co-substitution induced lattice expansion and enhanced crystallinity, unlike random doping, which caused lattice contraction and second-phase aggregation (Figure 6d). The co-substituted CZC also showed increased carrier mobility, reduced trap density, and improved operation stability. This work provides a strategy for designing stable, high-performance HPLSCs through rational doping via the Bridgman method.[38]

2.6. Other Methods

Beyond the conventional single-crystal growth techniques discussed above, novel methodologies have continued to emerge recently.

Yang et al. introduced a droplet-assisted self-alignment strategy to fabricate precisely patterned perovskite single-crystal arrays for high-performance optoelectronic devices, where the schematic diagram of the preparation process is shown in **Figure 7a**. Droplet-assisted self-alignment leverages gravity and surface tension to guide perovskite crystals to autonomously move, rotate, and align within suspended droplets under the vapor of an atypical antisolvent, formic acid. Crystals nucleate inside droplets or at liquid-gas interfaces, aligning with droplet edges to minimize surface energy. The demonstrated $MAPbBr_3$, $MAPbCl_3$, and $CsPbBr_3$ crystals achieved 95% alignment yield with pixel sizes ranging from 200 to 500 µm, where the area of the arrays was up to 10 cm × 10 cm, fabricated on diverse substrates (indium tin oxide, glass, quartz, polydimethylsiloxane (PDMS)) (Figure 7b–e). This work provides a low-cost, scalable, and substrate-agnostic approach to fabricating perovskite single-crystal arrays with unprecedented precision and uniformity.[39]

Niu et al. introduced a novel close-to-equilibrium crystallization (CEC) method to address the long-standing challenge of growing large, high-quality perovskite single crystals, which typically suffer from performance degradation as their size increases. As shown in Figure 7f, the CEC system consists of a solution supply unit, a crystal growth unit, and a solution recycling unit. This setup ensures constant solution concentration and temperature uniformity during growth by continuously replenishing fresh precursor and recycling depleted solutions. By optimizing solute feeding rates and maintaining thermal stability (±0.44 °C temperature difference), the system locks the growth process within the narrow thermodynamic window of perovskite crystallization, avoiding nucleation bursts or dissolution. As a result, the CEC method produced a large-scale, high-quality $FAPbBr_3$ HPLSC with dimensions of $51 \times 45 \times 10$ mm^3, the largest reported for $FAPbBr_3$ (Figure 7g).[40]

Recently, Saidaminov et al. introduced a pioneering Flux-Regulated Crystallization (FRC) method, which enabled reproducible high-quality perovskite single crystals by flux-regulated crystallization with a feedback loop. The FRC could directly control crystal growth rate in real-time by using camera-based size monitoring and a PID feedback loop to dynamically regulate solvent infusion (via syringe pump), maintaining stable linear growth for extended periods (>40 h) to yield high-quality single crystals (Figure 7h). This method overcame a fundamental limitation in traditional solution-based crystal growth, where growth rate control was indirect and unstable, enabling a systematic study of crystallization kinetics and the synthesis of HPLSCs with record crystal quality.[41]

Table 1 reveals critical trade-offs in HPLCS growth technologies. Solution-based methods (TLC/ITC/SSE/AVC) offer low-temperature processing (< 150 °C) and moderate scalability (several crystals/run), but face inherent limitations in industrial translation: 1) high solvent consumption (DMF/DMSO) leading to high costs, 2) stochastic nucleation causing high yield variations, and 3) thickness constraints (< 10 mm) restricting high-energy radiation absorption. Melt-growth techniques like Bridgman enable centimeter-thick crystals (>10 mm) vital for X- or γ-ray detectors, yet suffer from energy-intensive operation (400–600 °C) and phase segregation risks during slow cooling. Crucially, emerging closed-loop systems, CEC and FRC, address these bottlenecks through real-time supersaturation control (FRC) and continuous solution replenishment (CEC), achieving superior defect suppression while enhancing dimensions. However, industrial adoption demands further CAPEX reduction and advanced growth paradigms that synergistically boost throughput while ensuring crystallographic perfection and overcoming persistent bottlenecks in scalable production.

3. Optical Radiation Detection

3.1. Basic Parameters of Optical Radiation Photodetectors

3.1.1. Responsivity (R)

Responsivity is a critical performance metric for photodetectors, quantifying their ability to convert incident optical power into an electrical output signal. It is the ratio of the photodetector's output current (or voltage) to the incident optical power at a specific wavelength. Mathematically, it is expressed as:

$$R = \frac{I_p}{\Phi S} \tag{1}$$

where I_p is the photocurrent, Φ is the light intensity, and S is the active area of the photodetector.

Responsivity directly reflects the detector's sensitivity to light. A higher R indicates that the device generates a stronger electrical signal (current or voltage) per unit of incident optical power. This is crucial for weak light detection applications, such as low-light imaging or optical communications.

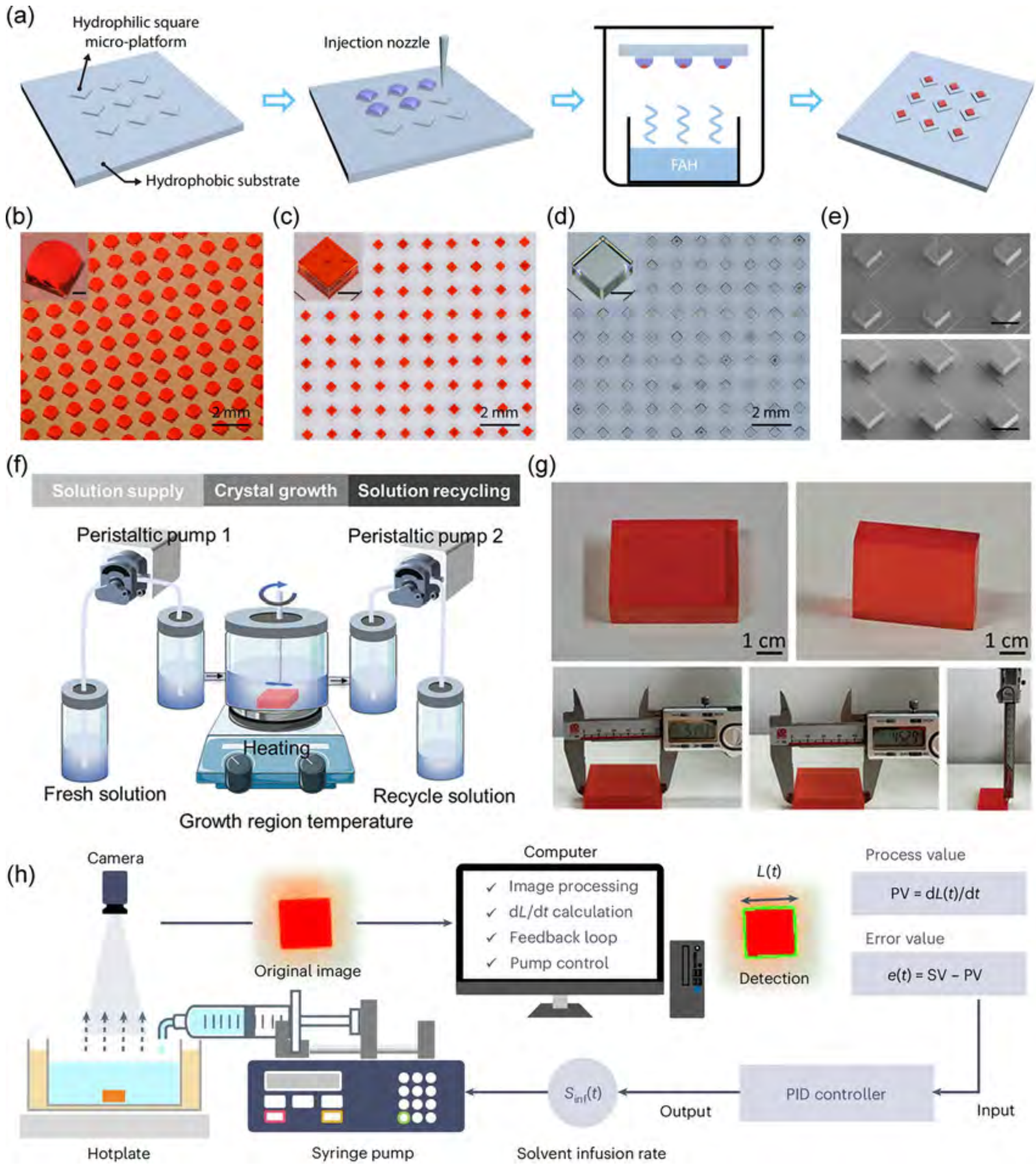

Figure 7. a) Schematic diagram of the preparation process of perovskite single-crystal arrays. Formic acid vapor-assisted crystallization was applied. b–d) Stereomicroscope images of the dyed red square precursor droplets b), as-grown $MAPbBr_3$ crystals c), and $MAPbCl_3$ crystals d). Insets show the detail of the precursor droples, the scale bars are 200 µm. e) Scanning electron microscopy images of the $MAPbBr_3$ and $MAPbCl_3$ crystals. The scale bars are 500 µm.[39] Copyright 2024, The American Association for the Advancement of Science. f) Schematic illustration of the equipment for close-to-equilibrium crystallization. g) Pictures of the $FAPbBr_3$ HPLSC.[40] Copyright 2025, John Wiley and Sons. h) Schematic of the FRC system.[41] Copyright 2024, Springer Nature.

3.1.2. External Quantum Efficiency (EQE)

The EQE of a photodetector quantifies the ratio of the number of charge carriers (electrons or holes) generated and collected by the device to the number of incident photons at a specific wavelength. It is expressed as:

$$EQE = \frac{hcR}{e\lambda} \tag{2}$$

where c is the speed of light, h is Planck's constant, R represents the responsivity of the photodetector, and e is the elementary charge. λ is the wavelength of the incident light.

The EQE quantifies a photodetector's ability to convert incident photons into usable electrical current, accounting for optical losses and carrier collection efficiency. It is a vital metric for evaluating material suitability, device design, and performance in applications ranging from solar energy harvesting to biomedical imaging. Maximizing EQE requires optimizing light absorption, minimizing losses, and enhancing charge transport.

Table 1. Comparative analysis of HPLSCs growth methods.

Methods	Type of source used	Temperature growth [°C]	Range of lateral size [mm]	Range of thickness [mm]	Growth duration [h]
TLC	Solution	25–150	Several to tens	1–10+	Tens to hundreds
ITC	Solution	25–100	Several to tens	1–10+	Several to Tens
SSE	Solution	25–90	Several	Several	Tens to hundreds
AVC	Solution	25–70	Several	Several	Tens to hundreds
Bridgman	Solid	Several hundreds	Tens	Hundreds	Tens to hundreds
CEC	Solution	Tens	Tens	10	Tens
FRC	Solution	40	Several	Several	Tens

3.1.3. On/Off Ratio

A photodetector's on/off ratio is the ratio of the photocurrent (I_p) generated under illumination to the dark current (I_d) measured in the absence of light. Mathematically, it is expressed as:

$$\text{On/off ratio} = \frac{I_p}{I_d} \tag{3}$$

The on/off ratio is critical for evaluating a photodetector's ability to differentiate between illuminated and dark states. It reflects the balance between photoresponse efficiency and noise suppression, directly impacting performance in applications requiring high sensitivity and low noise. Optimizing this ratio involves material selection, defect engineering, and device architecture design to maximize photocurrent while minimizing dark current.

3.1.4. Signal-to-Noise Ratio (SNR)

SNR is a dimensionless metric that quantifies the ratio of the strength of a desired electrical signal (generated by incident light) to the background noise in a photodetector. It is mathematically defined as:

$$SNR = \frac{I_p}{I_{noise}} \tag{4}$$

where I_noise represents the root-mean-square (RMS) noise current, and I_p is the photocurrent.

SNR quantifies a photodetector's ability to distinguish meaningful optical signals from inherent noise. It is pivotal for applications requiring high sensitivity and precision, such as biomedical imaging, environmental sensing, and quantum technologies. Optimizing SNR involves balancing material properties, device architecture, and noise mitigation strategies.

3.1.5. Noise Equivalent Power (NEP)

NEP is the minimum incident optical power required for a photodetector to generate an output signal equal to its intrinsic noise level. In other words, when the incident light power equals the NEP, the signal-to-noise ratio (SNR) becomes 1, meaning the signal is indistinguishable from the noise. Mathematically, NEP is defined as:

$$NEP = \frac{I_{noise}}{R} \tag{5}$$

where I_noise represents the RMS noise current, and R is the responsivity of the detector.

NEP quantifies the weakest detectable optical signal a photodetector can resolve. A lower NEP indicates higher sensitivity, enabling the detection of fainter light signals (e.g., in astronomy or biomedical imaging).

3.1.6. Detectivity (D^*)

Detectivity is a critical figure of merit for photodetectors, quantifying their ability to detect weak optical signals. It normalizes the detector's sensitivity to noise characteristics and active area, enabling a standardized performance comparison across devices with different sizes and operating conditions. Detectivity is defined as:

$$D^* = \frac{\sqrt{S\Delta f}}{NEP} \tag{6}$$

where S is the active area of the photodetector, and Δf represents the electrical bandwidth.

Detectivity quantifies a photodetector's ability to resolve weak optical signals by balancing responsivity, noise, and physical dimensions. Achieving high D^* requires minimizing noise while maximizing responsivity through efficient photon-to-carrier conversion.

3.1.7. Linear Dynamic Range (LDR)

The LDR of a photodetector quantifies the range of incident optical power over which the detector's output signal maintains a linear relationship with the input power. It is defined as the ratio of the maximum to the minimum detectable optical power, typically expressed in decibels (dB):

$$LDR \quad (dB) = 10\log\frac{P_{max}}{P_{min}} \tag{7}$$

where P_max represents the maximum optical power at which the detector's response remains linear (beyond this, saturation or nonlinear distortion occurs), $P_{\min}$ represents the minimum detectable optical power, often equivalent to the NEP, where the signal equals the noise floor.

The LDR characterizes a photodetector's ability to linearly convert optical power into electrical signals over a wide intensity range. It combines noise performance ($P_{\min}$) and saturation limits ($P_{\max}$), making it essential for applications requiring accurate signal detection across varying light conditions. Optimizing LDR involves balancing material properties, noise reduction, and thermal management to achieve both sensitivity and robustness.

3.1.8. Response Speed

A photodetector's response speed (or response time) refers to the time it takes to generate and stabilize an electrical output signal in response to a change in incident light intensity. It quantifies how quickly a detector can track rapid variations in optical signals. Response speed is typically characterized by two key parameters:

1) Rise time: The time required for the output signal to increase from 10% to 90% of its maximum value when the light is turned on.
2) Fall Time: The time required for the output signal to decrease from 90% to 10% of its maximum value when light is turned off.

The response speed of a photodetector defines its ability to resolve rapid optical signal changes, governed by material properties, device design, and operating conditions. Fast response is critical for high-frequency applications, while slower detectors may prioritize sensitivity or cost-effectiveness. Balancing speed with other performance metrics is essential for optimizing detectors across diverse fields, from telecommunications to biomedical imaging.

3.1.9. Photoconductive Gain (G)

Photoconductive gain refers to the ratio of the photogenerated current in a photodetector to the theoretical maximum current if each incident photon produced only one electron-hole pair. It quantifies the amplification of electrical output due to the photoconductive effect, where light-induced carriers contribute multiple times to the current flow. Mathematically, it is expressed as:

$$G = \frac{\mu \tau V}{L^2} \tag{8}$$

μ is the carrier mobility, τ is the carrier lifetime, V is the applied bias voltage, and L is the inter-electrode spacing.

Photoconductive gain quantifies the photocurrent amplification in detectors where light-induced carriers contribute multiple times to the electrical output. It is governed by material properties (mobility, lifetime), device geometry, and operating conditions (bias voltage). Crystallographic defects also play a dual role in photoconductive gain dynamics. While defects typically degrade mobility (μ), deep-level traps can significantly prolong effective carrier lifetime (τ) through repetitive trapping-detrapping cycles. This occurs when carriers are intermittently captured by trap states and subsequently released before recombination, effectively extending their contribution to photocurrent.[24] However, excessive trap densities induce gain-noise trade-offs, where rising G is counterbalanced by recombination noise that degrades detectivity (D*). This defect-mediated gain mechanism, termed trap-assisted photoconduction, has been experimentally validated as a dominant factor in perovskite detectors.[26]

While high gain enhances sensitivity for weak-light detection, it must be balanced against noise and saturation effects. Understanding and optimizing photoconductive gain is critical for designing detectors tailored to night vision, optical communications, and scientific instrumentation applications.

3.2. Architectures of Optical Radiation Photodetectors

Photodetectors are categorized into photothermal and photonic types based on operational principles. Photothermal detectors operate through radiation-induced thermal effects, where absorbed photons increase lattice vibrations and elevate semiconductor layer temperature, thereby modulating carrier concentration for detection. In contrast, photonic detectors utilize photon-generated electron-hole pairs to alter resistive states in the semiconductor layer. This fundamental distinction creates critical performance divergences between them: photothermal detectors exhibit wavelength-independent responsivity due to their thermal transduction mechanism, whereas photonic devices demonstrate wavelength selectivity dictated by semiconductor bandgap energy; besides, the thermal inertia of photothermal systems limits response speeds, while photonic detectors achieve nanosecond-scale responses through direct carrier generation. Accordingly, photonic detectors are preferred.

Photonic detectors are further classified into three architectures: photodiodes, which operate under reverse bias for fast response; photoconductors, which utilize photoconductive gain through persistent conductivity; and phototransistors, which enable gate-voltage-modulated carrier concentration tuning. The phototransistor configuration offers unique advantages in optimizing linearity and response speed through electrostatic control of channel conductivity. However, implementation with HPLSCs remains challenging due to their macroscopic dimensions (>1 mm^3)—the bulk crystal geometry prevents effective gate-field penetration, fundamentally limiting carrier density modulation efficiency. This physical constraint has resulted in scarce reports on HPLSC-based phototransistors. Given the current technological limitations in phototransistor implementation with bulk single crystals and the predominance of photodiode/photoconductor architectures in perovskite optoelectronics, this review concentrates explicitly on these two operational modalities.

3.2.1. HPLSC-Based Photodiodes

Photodiode operation leverages the photovoltaic effect, where illumination generates electron-hole pairs separated by the built-in electric field of semiconductor junctions, producing a reverse photocurrent proportional to incident light intensity. These devices manifest in three principal configurations: conventional p-n junctions utilizing doping-induced depletion layers, p-i-n structures with intrinsic layers for enhanced quantum efficiency, and Schottky-type designs exploiting work function mismatches at perovskite/electrode interfaces. Common advantages across architectures include near-unity carrier separation efficiency through drift-dominated transport, ultralow dark current densities, and sub-nanosecond response times enabled by minimized junction capacitance.

While vertical architectures remain the predominant configuration in photodiodes, lateral-configuration photodiodes based on HPLSCs have also been reported. Prochowicz et al. achieved one HPLSC p-n junction by controlling the epitaxial growth of Ag^+-doped $MAPbBr_3$ on Sb^{3+}-doped $MAPbBr_3$, ensuring minimal lattice mismatch and continuous band alignment (**Figure** 8a). Combined with asymmetric Ag/Pt electrodes, this photodiode demonstrated record-high self-powered metrics at zero bias: open-circuit voltage: 0.95 V (among the highest for $MAPbBr_3$-based devices), responsivity: 0.41 A W^{-1} at 530 nm, and detectivity: 6.39×10^{11} Jones (Figures 8b,c). This work established a new paradigm for designing high-performance, self-powered HPLSC photodiodes.[42]

External field modulation enables dynamic control over carrier transport dynamics and photoresponse characteristics in photodiodes. Devan et al. synthesized $CH_3NH_3PbBr_3$ HPLSCs by the ITC method. The $CH_3NH_3PbBr_3$-based photodiodes fabricated by thermally depositing Ni and Ag electrodes on opposite sides of the HPLSC demonstrated a Schottky junction-driven self-powered operation (Figure 8d). Under white light illumination (720 lux), the device achieved a photocurrent of ≈3 $\mu A\cdot cm^{-2}$ at 5 V bias, with responsivity and detectivity values of ≈14 $mA\cdot W^{-1}$ and $\approx 5 \times 10^7$ Jones, respectively (Figures 8e,f). They then applied an external B-field (0–100 mT) to the device, which enhanced the photocurrent by ≈28% at 30 mT, with R and D^* rising to ≈37 $mA\cdot W^{-1}$ and $\approx 2 \times 10^8$ Jones. This improvement was attributed to reduced recombination and enhanced charge transport at the Ni/HPLSC interface, facilitated by trap-state passivation under the B-field.[43]

3.2.2. HPLSC-Based Photoconductors

Photoconductors employ a coplanar architecture with HPLSCs as photosensitive channels between lateral symmetric metal electrodes. The operational mechanism hinges on photogenerated carrier dynamics, where light-induced electron-hole pairs are separated and transported under an applied electric field, converting optical signals into electrical currents through a synergistic interplay of prolonged carrier lifetimes and accelerated transit times. The simplified fabrication process—utilizing scalable techniques like interdigitated electrode patterning with fractal designs—supports wafer-scale integration and achieves bias-adaptive dynamic ranges. All the advances position these devices as robust solutions for industrial imaging and optical interconnects.

Zhang et al. reported a synergistic nucleation and supersaturation-engineered method using methanol as the antisolvent to synthesize high-quality, millimeter-sized $Cs_3Bi_2X_9$ (X = Cl, Br, I) HPLSCs at low temperatures (≈50 °C) (Figure 8g). These HPLSCs were configured into photoconductors. The $Cs_3Bi_2Br_9$ HPLSC-based photodetector exhibited optimal performance with a high detectivity (7.37×10^{11} Jones), ultrahigh on/off ratio (5922), and fast carrier dynamics (lifetime ≈2.18 ns), surpassing previous reports for Bi-based perovskites (Figure 8h).[44]

Ji et al. synthesized high-quality $Cs_3Bi_2Br_9$ HPLSCs using the AVC method (Figure 8i). They then configured the HPLSC into a photoconductor (Figure 8j), which demonstrated record-fast response times for Bi-based perovskites with the rise time of 96 ms and decay time of 80 ms under 375 nm UV illumination (Figure 8k). The device also achieved a high responsivity of 1.958×10^{-5} A W^{-1}, outperforming many lead-free perovskite-based detectors.[45]

3.3. HPLSC-Based Photodetectors for Different Wavelengths

Photodetectors for optical radiation detection can typically be classified into three spectral regimes based on their operational wavelength ranges: visible-light photodetectors, ultraviolet (UV) photodetectors, and infrared (IR) photodetectors. Herein, we sequentially examine recent progress in these wavelength-specific photodetector categories, highlighting key advancements and emerging trends in their respective spectral domains.

3.3.1. HPLSC-Based Visible Light Photodetectors

Since the bandgaps of perovskite materials mainly fall within the visible spectrum, HPLSCs are highly suitable for visible light photodetectors. Recent advances have focused on crystal engineering and device architecture innovations to optimize performance.

Wang et al. presented a novel method for the in situ growth of $MAPbBr_3$ HPLSCs on a transport layer using cesium(I) bis(trifluoromethanesulfonyl)imide (CsTFSI) ionic liquid (**Figures** 9a,b). ThCs$^+$ ions were incorporated into the $MAPbBr_3$ lattice, reducing its formation energy and facilitating crystal growth. $TFSI^-$ anions coordinated with Pb^{2+} via lone-pair electrons of oxygen, passivating Pb dangling bonds and reducing defect density (trap density was 5.39×10^{11} cm^{-3}) (Figure 9c–e). The HPLSCs fabricated by this method also showed improved carrier mobility (0.84 $cm^2\cdot V^{-1}\cdot s^{-1}$, Figure 9d) and thermal stability. The corresponding photodetector showed high responsivity of 0.33 A W^{-1}, detectivity of 3.61×10^{11} Jones, and fast response speed of 1.22/0.57 µs. This work provided a scalable, defect-engineering strategy to grow high-quality HPLSCs for visible light photodetectors.[46]

Designing and constructing HPLSC-based heterostructures is also promising for achieving high-performance photodetectors. Zhou et al. developed a self-powered $CsPbBr_3/SrTiO_3$ all-single-crystal heterojunction photodetector for optical communication systems. $CsPbBr_3$ HPLSCs were synthesized via the ITC method, while heterojunctions were fabricated using a low-temperature surface reconstruction method to bond crystals with minimal lattice mismatch (0.47%) (Figure 9f). The optimized device ($Au/CsPbBr_3/Nb{:}SrTiO_3$/Graphene) achieved record self-powered performance: high responsivity (1.1 mA W^{-1} at 500 nm, 0 V), ultrafast response (0.29 µs rise/31 µs decay), and wide spectral response (350-550 nm) (Figure 9g).[47]

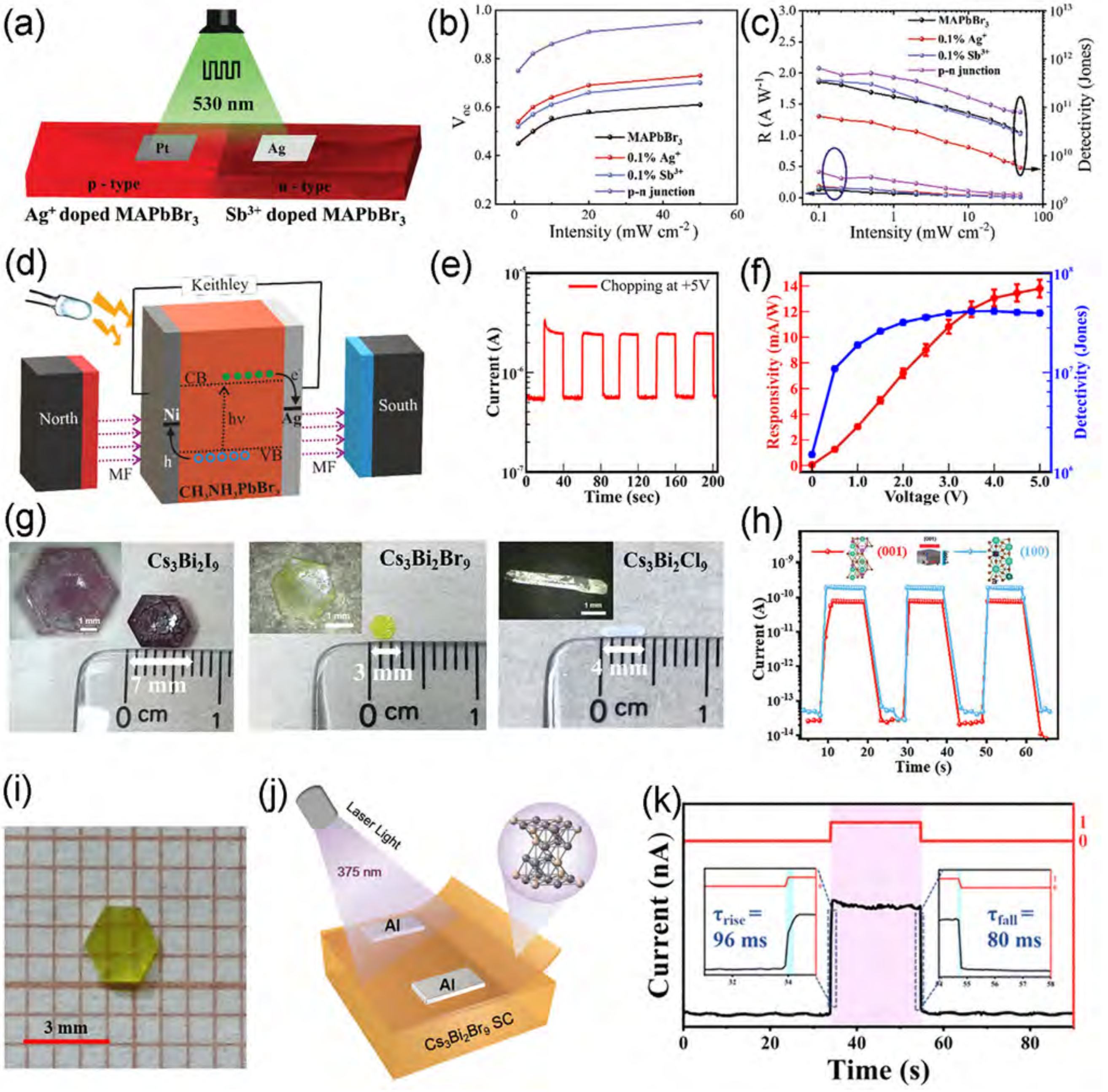

Figure 8. a) Schematic illustration of the self-powered p-n junction photodiode based on metal-doped MAPbBr$_3$ HPLSC with the asymmetric metal electrodes. b) The photovoltage of the self-powered photodetector under different light intensities at zero bias. c) Responsivity (left axis) and specific detectivity (right axis) of the self-powered photodetector.[42] Copyright 2023, John Wiley and Sons. d) Schematic of a capacitor-like structured Ag/MAPbBr$_3$ HPLSC/Ni device. e) Transient photoresponse at a bias potential of +5 V with light pulses of 20 s, and (f) responsivity and detectivity of Ag/MAPbBr$_3$ HPLSC/Ni device.[43] Copyright 2024, American Chemical Society. g) Optical photos of Cs$_3$Bi$_2$X$_9$ (X = I, Br, Cl) HPLSCs. h) *I-t* curves of different crystal faces of Cs$_3$Bi$_2$Br$_9$ HPLSC.[44] Copyright 2024, John Wiley and Sons. i) A Cs$_3$Bi$_2$Br$_9$ HPLSC grown by the AVC method. j) The structure diagram of the photoconductor device prepared by the Cs$_3$Bi$_2$Br$_9$ HPLSC. k) The light current curve and the photo response time are in the on and off states (the inset graph).[45] Copyright 2024, Royal Society of Chemistry.

Some other HPLSCs-based heterojunctions have also been proposed to improve the performance of the photodetectors. Cong et al. presented a high-performance self-powered broadband imaging photodetector based on a single-crystal CsPbBr$_3$/single-crystal β-Ga$_2$O$_3$ heterojunction. The device is the first reported heterojunction photodetector fabricated using single-crystal CsPbBr$_3$ and single-crystal β-Ga$_2$O$_3$. The CsPbBr$_3$ HPLSC was synthesized using the ITC method. The type-II band alignment of the heterojunction generates a built-in electric field (0.87 V), enabling zero-bias operation. This eliminates

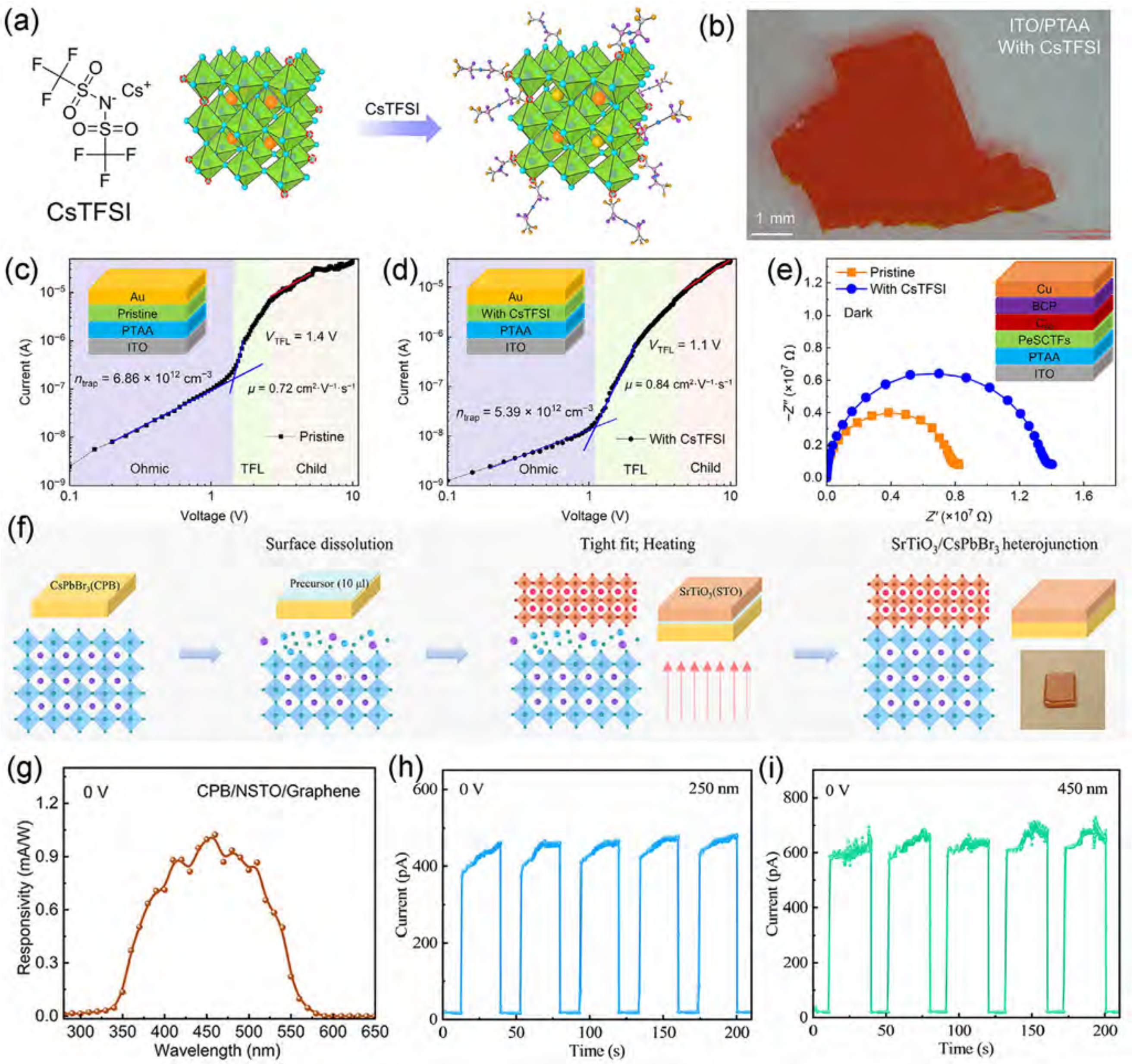

Figure 9. a) The structural formula of CsTFSI ionic liquid and the crystal structure diagram of $MAPbBr_3$ before and after adding CsTFSI. b) Microscopic image of $MAPbBr_3$ HPLSCs with CsTFSI. I-V curve of c) $MAPbBr_3$ HPLSCs and d) $MAPbBr_3$ HPLSCs with CsTFSI using the SCLC method. e) The impedance spectroscopy of the photodetector.[46] Copyright 2025, Tsinghua University Press. f) Schematic diagram of the low-temperature surface reconstruction method. g) Response spectra at 0 V for the Au/$CsPbBr_3$/Nb:$SrTiO_3$/Graphene photodetector.[47] Copyright 2025, John Wiley and Sons. On-off photoresponse of the $CsPbBr_3$/β-Ga_2O_3 photodetectors under 250 nm (h) and 450 nm (j) illumination.[48] Copyright 2024, Optica Publishing Group.

the need for external power, making the device energy-efficient and suitable for portable applications. The device achieves dual-band responsivity at 250 nm (7.9 mA W^{-1}) and 450 nm (6.5 mA W^{-1}), covering deep UV (solar-blind) to visible light (Figure 9h,i). This is attributed to the complementary absorption of β-Ga_2O_3 (4.8 eV bandgap) and $CsPbBr_3$ (2.27 eV bandgap). Demonstrates rapid response times: rise time < 1 µs and decay time < 50 µs under both UV (266 nm) and visible (532 nm) light. This work provides a novel strategy for designing self-powered, broadband photodetectors using HPLSC-based heterojunctions[48]

3.3.2. HPLSC-Based UV Photodetectors

UV photodetectors, particularly solar-blind deep UV photodetectors, hold critical importance in civilian and defense technologies—from missile plume detection and secure naval

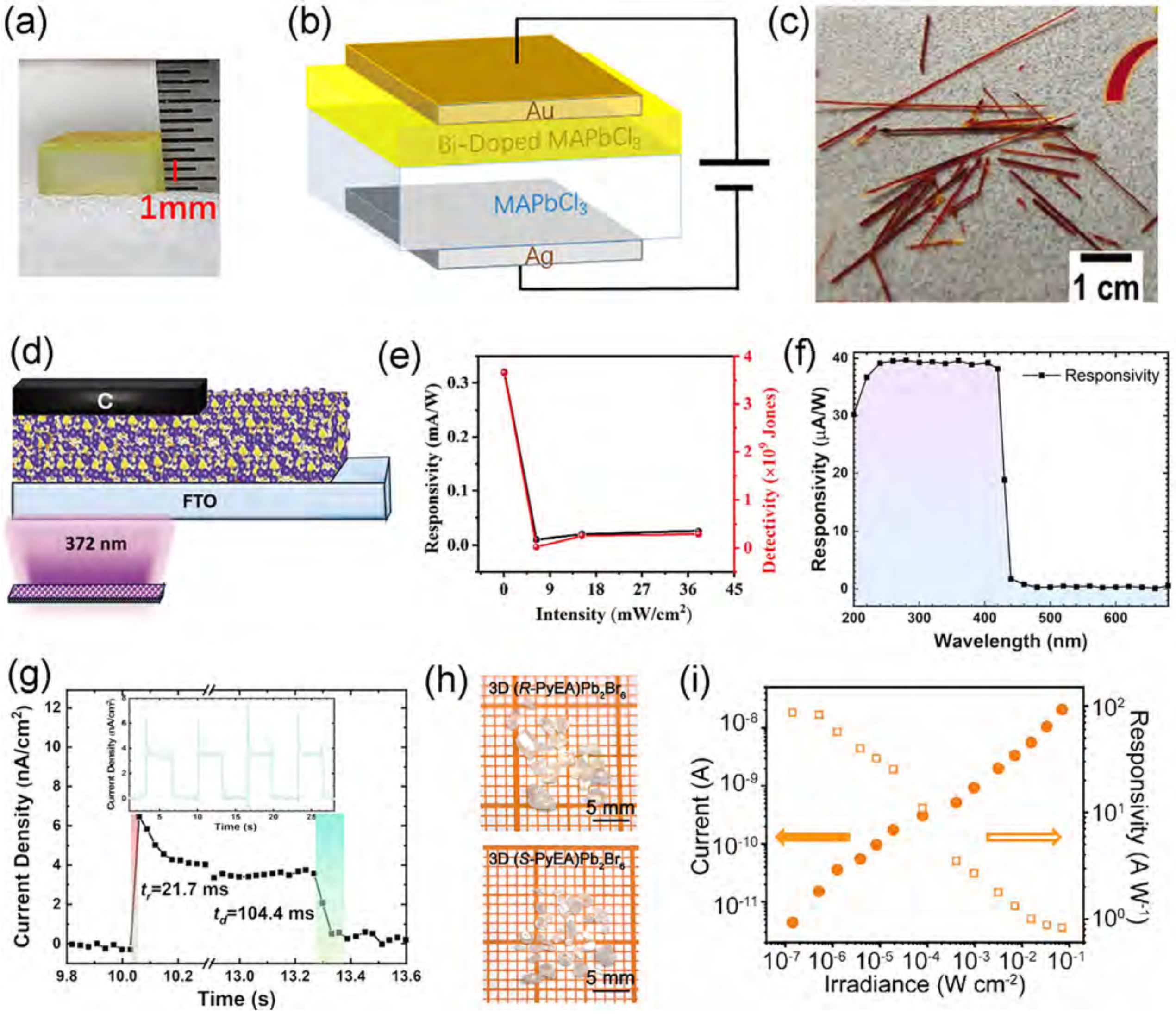

Figure 10. a) Optical photo of $MAPbCl_3$ HPLSC with Bi-doped $MAPbCl_3$ epitaxial layer. b) Schematic of the photodiode structure.[55] Copyright 2021, Frontiers Media S.A. c) HPLSCs of $Cs_3Cu_3Cl_9$ grown after adding HCl. d) The device structure of the FTO/Photoactive layer/C UV photodetector. e) Responsivity and specific detectivity for the device structures, FTO/$Cs_3Cu_2I_5$/C, and FTO/$Cs_3Cu_3Cl_9$/C under 372 nm.[56] Copyright 2025, John Wiley and Sons. f) The responsivity of a $Cs_3Sb_2Cl_9$ HPLSC photodetector as a function of wavelength. g) Single photocurrent response cycle with light irradiation ON and OFF. The inset is the time response of the photodetector.[57] Copyright 2024, Royal Society of Chemistry. h) Photographs of (R-PyEA)Pb_2Br_6 and (S-PyEA)Pb_2Br_6 perovskite HPLSCs. i) The irradiance-dependent photocurrents and responsivities of the (R-PyEA)Pb_2Br_6 device under unpolarized 365 nm illumination.[58] Copyright 2024, American Chemical Society.

communications to sterilization monitoring and early skin cancer diagnosis.[16,49] Most conventional 3D halide perovskites (ABX_3) face inherent limitations for UV detection due to their visible-range bandgaps (1.5–2.3 eV), prompting strategic material engineering approaches. Ion doping has emerged as an effective pathway to tailor perovskite optoelectronics.[50] In addition, low-dimensional halide perovskites (2D/1D/0D) exhibit quantum confinement effects that systematically widen their bandgaps, enabling direct UV detection.[51–54] This section presents and analyzes recent breakthroughs in HPLSC-based UV detectors.

Some pure HPLSCs with high quality and a suitable bandgap are good candidates for UV detectors. Shen et al. synthesized $MAPbCl_3$ single crystals with 3–6 mm sizes using a two-step ITC method, which shows low defect density ($\approx 7.9 \times 10^9$ cm^{-3}) and high carrier mobility (64 cm^2 V^{-1} s^{-1}). The UV photodetectors based on it showed good performance and storage stability, where the responsivity is as high as 3.73 A W^{-1} at the wavelength of 415 nm.[59]

Doping is one effective strategy to achieve high-performance HPLSC-based UV detectors. Lei et al. fabricated an epitaxial Bi-doped $MAPbCl_3$ layer on $MAPbCl_3$ single crystals, obtaining an n/n+ junction by the ITC method (**Figure 10a**). The photodiode of the n/n+ junction shows a low dark current density of −2.15 μA cm^{-2} at −20 V bias voltage with the responsibility of 404.7 mA W^{-1} and detectivity of 4.87×10^{11} Jones at 393 nm, where the device structure is shown in Figure 10b. Remarkably, the response speed of the device reached 176.3 ns at −200 V bias, which was the fastest responding $MAPbCl_3$ photodetector at that time.[55]

Cu-based HPLSCs have recently been widely studied. Batabyal et al. developed a facile strategy to grow $Cs_3Cu_3Cl_9$ bulk single crystals from $Cs_3Cu_2I_5$ microcrystals with the assistance of HCl (Figure 10c). Then, a self-powered UV photodetector with the structure of FTO/$Cs_3Cu_3Cl_9$/C was fabricated (Figure 10d), where the responsivity of 0.13 mA W^{-1} and detectivity of 2.2×10^9 Jones were achieved under UV illumination of wavelength 372 nm at 0 bias voltage (Figure 10e).[56]

Some new HPLSCs have also been synthesized for high-performance photodetectors. Luo et al. presented a new 2D bilayered DJ-type halide perovskite $(3AMPY)EAPb_2Br_7$ with aromatic diammonium (3AMPY) as the interlayer spacer. The aromatic diammonium spacer enables a shorter interlayer distance (3.561 Å) and enhanced rigidity, minimizing lattice distortion and improving carrier transport. Large single crystals were grown and configured into photodetectors. Owing to the excellent photoelectric properties of this 2D halide perovskite, the device exhibits an impressive photodetection ability from UV (377 nm) and visible (405 nm) to near-infrared (800 nm). The responsivity at the wavelength of 405 nm reached 827.4 mA $W^{-1,}$ and the detectivity.[60]

Wang et al. presented a novel approach to synthesizing centimeter-sized, lead-free $Cs_mSb_nCl_{m+3n}$ perovskite single crystals for high-performance visible-blind UV photodetectors. A hybrid solvent of dimethyl sulfoxide (DMSO) and hydrochloric acid (HCl) significantly enhances the solubility of CsCl and SbCl precursors, enabling the growth of high-quality α-$Cs_3Sb_2Cl_9$ and $Cs_5Sb_2Cl_{11}$ single crystals via a gradient cooling method. The crystals exhibit excellent crystallinity, with optical bandgaps of 2.86 eV (α-$Cs_3Sb_2Cl_9$) and 2.98 eV ($Cs_5Sb_2Cl_{11}$), making them ideal for UV detection. High transmittance (>87%) and low defect density further validate their optoelectronic potential. The photodetector demonstrates ultralow dark current density (91 pA cm^{-2}), high UV/visible rejection ratio ($R_{360}/R_{480} = 150$, Figure 10f), fast response speeds (21.7 ms rise, 104.4 ms decay), and robust stability under ambient conditions (Figure 10g).[57]

Polarized UV photodetectors can also be achieved using chiral HPLSCs. Wu et al. reported a wafer-scale integration of chiral 3D perovskite HPLSCs for high-performance full-Stokes polarimeters (Figure 10h). A novel chiral 3D perovskite, $(R/S\text{-}PyEA)Pb_2Br_6$, was synthesized using rationally designed chiral cations (R/S-1-(pyridine-4-yl)ethan-1-amine): a one-step fabrication method was developed to create long-range oriented, defect-free single-crystal microwire arrays on Au substrates. This technique leverages asymmetric wettability templates and solvent evaporation dynamics to achieve wafer-scale patterning (up to 4-inch substrates) with precise alignment and uniformity. The corresponding polarized UV photodetector achieves record-breaking performance with a responsivity of 86.7 A W^{-1} (Figure 10i), detectivity of 4.84×10^{13} Jones, rise/decay times of 428.0 µs/141.6 µs, and a circular-/linear-polarization anisotropy factor of 0.42/1.52, under 365 nm light.[58]

3.3.3. IR Detectors

IR photodetectors play pivotal roles in advanced technologies, such as non-invasive health diagnostics, industrial process monitoring, deep-space optical communications, etc.[61,62] However, as we know, conventional halide perovskites—including low-dimensional and lead-based 3D variants—exhibit bandgaps that fundamentally limit their optical response to wavelengths below 850 nm. To circumvent this spectral constraint, researchers have to develop new strategies. For example, utilizing surface trap states in intentionally undercoordinated perovskite lattices facilitates sub-bandgap absorption via mid-gap defect transitions. Besides, tin-based 3D perovskites like $MASnI_3$ can be directly used in IR detection owing to their narrow bandgaps of ≈1.4 eV. Yet, their practical deployment faces critical challenges: Sn^{2+} oxidation to Sn^{4+} under ambient conditions induces rapid performance degradation.[63,64] Herein, recent achievements in HPLSCs-based IR detectors are presented.

High-quality 3D halide perovskite $MAPbI_3$ can be used in NIR detection. Tan et al. synthesized $MAPbI_3$ HPLSCs with low trap density ($n_{trap} = 8.7 \times 10^8$ cm^{-3}) and strong absorption up to 840 nm via the ITC method (**Figure 11a**). The corresponding NIR photodetector achieved 1.33 A W^{-1} responsivity and 2.18×10^{12} Jones detectivity at 780 nm under 5 V bias (Figure 11b,c). Besides, since the cutoff wavelength of the HPLSCs is 840 nm, it is ideal for NIR light detection in the first biological window. A custom-built NIR imaging system was integrated using the photodetector with an optical microscope (Figure 11d), enabling high-energy and spatial resolution imaging. This work validates the potential of $MAPbI_3$ HPLSCs as high-performance, cost-effective NIR photodetectors for biomedical imaging.[65]

Perovskites primarily exhibit bandgaps in the UV–vis range, with very few possessing intrinsic infrared absorption. Therefore, band engineering to broaden the absorption spectrum of HPLSCs serves as the primary approach for achieving infrared detection.[68,69] Trap states in HPLSCs can regulate the band structure, representing an effective means to achieve absorption in the infrared band. Trap states in HPLSCs can induce NIR absorption. Sun et al. presented a TLC method to fabricate $Cs_2NaInCl_6$ (CNIC) HPLSCs and constructed hetero-crystals (CNIC/CNIC-Sb(V), Figure 11e). The Sb^{5+} substitution for In^{3+} induced charge imbalance, generating Na^+ vacancies (color centers) to maintain charge neutrality. The Na^+ vacancies and Frenkel defects synergistically created localized trap states, significantly enhancing NIR absorption up to 1300 nm. The hetero-crystal-based infrared photodetectors exhibited self-driven photoresponse under zero bias (the device structure is shown in Figure 11f, and the energy level diagram is shown in Figure 11g), achieving a D^* of 1.28×10^{12} Jones and responsivity R of 5.3 nA W^{-1} at 1310 nm. The study underscores the potential of defect engineering and heterostructure design in HPLSC-based infrared photodetectors.[66]

In addition, mixed-cation perovskites also serve as an effective approach for tuning bandgaps and enabling infrared detection. Recently, tin-based HPLSCs have demonstrated significant advancements in IR detection. Chu et al. achieved a vertical bandgap-graded structure in Pb-Sn alloyed HPLSCs ($Cs_{0.1}FA_{0.87}GA_{0.03}Pb_{1\text{-}x}Sn_x(I_{0.95}Br_{0.05})_3$) by introducing a novel

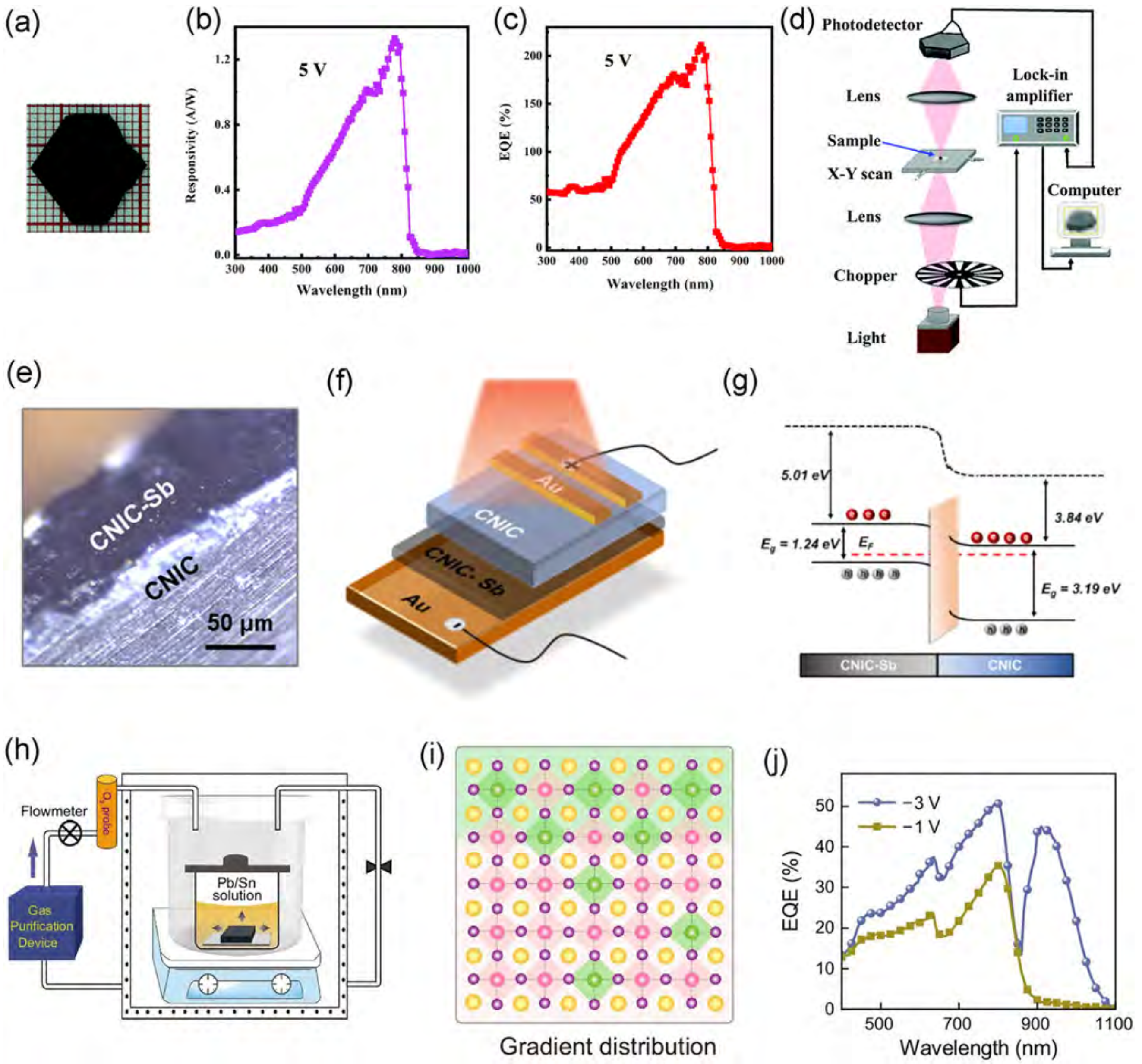

Figure 11. a) Photograph of the $MAPbI_3$ HPLSC. Responsivity b) and EQE c) of the photodetector based on the $MAPbI_3$ HPLSC at 5 V. d) Light path diagram of the microscopic imaging system.[65] Copyright 2022, Royal Society of Chemistry. e) Optical photograph showcasing the profile of the hetero-crystal. f) Schematic view of the CNIC/CNIC-Sb photodetector device. g) Energy level diagram of CNIC/CNIC-Sb hetero-crystal with equilibrium state.[66] Copyright 2025, Elsevier. h) Illustration of the system to prepare Pb–Sn perovskite crystals under different surrounding atmospheres. i) Schematics showing the Pb–Sn alloyed gradient structures. j) EQE of the Pb–Sn perovskite photodetector under different biases.[67] Copyright 2024, Springer Nature.

flow-through environmental chamber to control oxygen through the ITC method (Figure 11h). During the crystal growth, oxygen interacted with Sn^{2+}, promoting vertical compositional gradients (Sn-rich surface, Pb-rich bulk) while suppressing Sn oxidation and defect formation (Figure 11i). This gradient structure enhances carrier mobility (electron mobility up to 293 $cm^2\ V^{-1}\ s^{-1}$) and generates a built-in electric field, improving charge separation and operation stability. At low bias (−1 V), this Pb-Sn alloyed HPLSCs-based photodetector primarily detected visible light (peaking at 800 nm), while increasing the bias (−3 V) activated a second response peak in the NIR region (up to 1100 nm) (Figure 11j). The device achieved a record LDR of 177 dB, a high detectivity (1.3×10^{12} Jones at 800 nm), and a fast response speed (46.4 kHz cutoff frequency). The HPLSCs-based photodetector was also integrated seamlessly with Bayer filters, which delivered excellent color fidelity under infrared interference and 26-bit grayscale resolution in NIR mode. This work opened an effective design strategy for

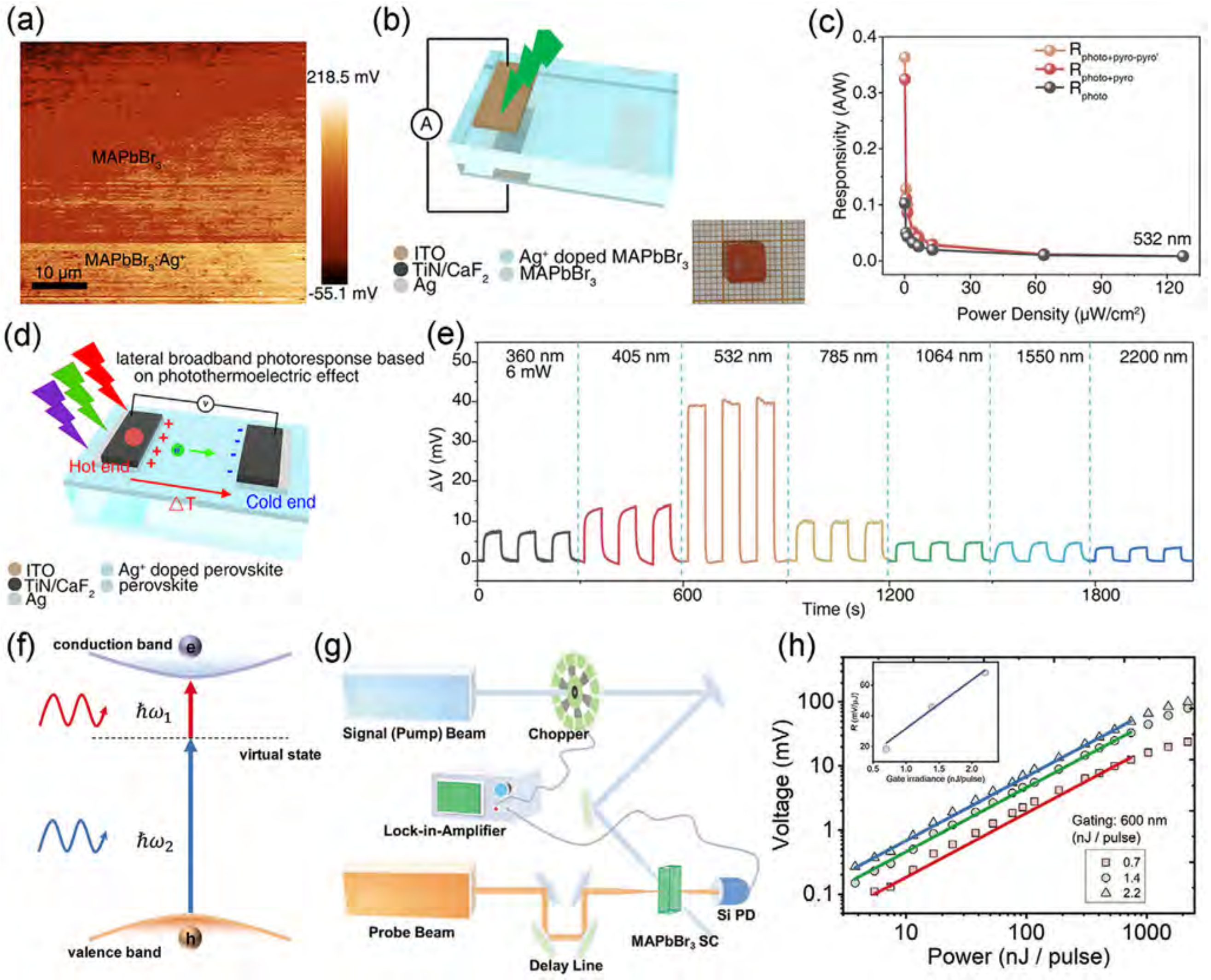

Figure 12. a) Contact potential difference image a of Ag^+ doped treated $MAPbBr_3$ HPLSC's surface by KPFM measurement. b) The schematic diagram of a $MAPbBr_3$-based vertical narrowband photodetector. Inset: the photograph of the real device. c) The zero-bias responsivities of the vertical photodetector as a function of the power density. d) Schematic diagram of a broadband photodetector based on lateral photothermoelectric. e) The photothermoelectric voltage response of the lateral broadband photodetector under 360–2200 nm laser illumination with a power of 6 mW.[70] Copyright 2025, John Wiley and Sons. f) Schematic diagram of ND-TPA. g) Schematic diagram of the infrared photon detection method using the strong ND-TPA of $MAPbBr_3$ HPLSC and a Si photodetector. h) The output voltage versus the input infrared pulse power. Inset: the responsivity versus the probe power.[71] Copyright 2022, John Wiley and Sons.

HPLSC-based IR photodetectors and high-performance imaging systems.[67]

By designing novel device structures, the detection range of HPLSCs can also be extended into the infrared band, enabling multi-band detection. Guo et al. presented a dual-modal perovskite single-crystal photodetector that integrates vertical pyro-phototronic effects (IPPE) and lateral photothermoelectric effects (PTEE) to achieve narrowband and broadband detection. $MAPbX_3$ (X = Cl, Br, I) HPLSCs were synthesized via the ITC method. $MAPbBr_3$ HPLSC's surface was then treated with AgBr to form vertical p-n junctions and enhance conductivity (**Figure 12a**). The vertical narrowband detection utilizes charge collection narrowing and IPPE, achieving narrowband response (FWHM ≈ 113 nm) with peak responsivity (0.36 A W^{-1} at 532 nm) and fast response (77 μs rise/157 μs fall) (Figures 12b,c). The lateral broadband detection relies on PTEE induced by thermal gradients, enabling ultrawide spectral response (360–2200 nm) with a responsivity of 0.493 V W^{-1} at 2200 nm (Figures 12d,e). This work offers a low-cost, scalable solution to bridge the gap between narrowband precision and broadband versatility in photodetectors.[70]

Two-photon absorption (TPA) also serves as a critical detection mechanism for IR detection. Zhou et al. revealed that non-degenerate two-photon absorption (ND-TPA, Figure 12f), where two photons of different energies 0.73 eV) are absorbed, exhibited a significantly enhanced absorption coefficient of 51.3 cm GW^{-1}, approximately six times higher than degenerate TPA (D-TPA) coefficients in $MAPbBr_3$. Transient transmission dynamics

Table 2. Performance of HPLSC-Based Photodetectors for Optical Detection.

HPLSC	Growth method	Wavelength [nm]	R [mA W^{-1}]	D^* [Jones]	Rise/Fall time [ms]	Refs.
(N-MPDA)PbBr$_4$	SSE	405	1.24×10^5	10^{12}	100/100	[72]
CsCu$_2$I$_3$	AVC	360	276.94	1.34×10^{12}	0.37/1.08	[73]
(C$_{11}$H$_{18}$N)$_6$Sb$_7$I$_{27}$	AVC	365	15	2×10^{11}	0.6/3.0	[74]
Cs$_3$Bi$_2$Br$_9$	AVC	365	23.1	7.37×10^{11}	/	[44]
Cs$_3$Bi$_2$Br$_9$	AVC	375	0.01958	/	96/80	[45]
CsCuAgI$_3$	AVC	375	/	/	370/290	[75]
MAPbBr$_3$-MAPbBr$_3$@PbBr(OH)	AVC	520	31	4.8×10^{11}	48/64	[76]
(AEHB)$_2$SnBr$_6$	TLC	254	9960	6.8×10^{12}	341/416	[77]
Cs$_2$AgBiBr$_6$:Er	TLC	370	16.9	2.94×10^{10}	242/342	[78]
Cs$_2$FeCl$_5$·H$_2$O	TLC	397	8.41	4.43×10^6	7/7	[79]
(PA)$_2$PbBr$_4$	TLC	405	91.2	6.08×10^{12}	0.28/0.29	[80]
(3AMPY)(EA)Pb$_2$Br$_7$	TLC	405	827.4	8.67×10^{12}	0.347/0.256	[60]
(GA)(MA)$_2$Pb$_2$I$_7$	TLC	532	2540	3.04×10^{12}	/	[81]
Cs$_3$Bi$_2$I$_9$	ITC	525	0.03889	2.8×10^8	0.0015/0.0025	[82]
CsPbBr$_3$	ITC	555	420	6.26×10^{10}	40/35	[83]
MAPbI$_3$	ITC	790	660	3.37×10^{13}	0.000167/0.00017	[84]
Cs$_{0.1}$FA$_{0.87}$GA$_{0.03}$Pb$_{1\text{-}x}$Sn$_x$(I$_{0.95}$Br$_{0.05}$)$_3$	ITC	800	230	1.3×10^{12}	/	[67]
		940	340	3.7×10^{11}	0.032/0.165	

experiments validate the strong ND-TPA effect, attributed to resonance enhancement near the bandgap (2.33 eV). Then, a nonlinear IR photodetector was developed by integrating MAPbBr$_3$ HPLSCs with a silicon photodiode, where the device structure is shown in Figure 12g. The detector leverages ND-TPA in MAPbBr$_3$ to modulate the transmission of a visible probe beam (600 nm), which is then detected by the Si photodetector. The device achieves a detection limit of ≈1 nJ pulse^{-1} and responsivity of 68 V W^{-1} for 1700 nm femtosecond laser pulses (Figure 12h). Performance surpasses commercial pyroelectric/thermopile detectors and approaches that of HgCdTe detectors.[71]

Table 2 provides a comparative analysis of critical performance metrics for state-of-the-art HPLSC photodetectors reported recently.

4. Ionizing Radiation Detection

4.1. Basic Parameters of Ionizing Radiation Photodetectors

4.1.1. Sensitivity

The sensitivity of an ionizing radiation detector refers to its ability to detect and convert incident ionizing radiation (e.g., X-ray, γ-ray) into a measurable electronic signal with high efficiency and minimal noise. Quantitatively, it is often defined as the minimum detectable radiation flux (e.g., photons per unit area and time) required to produce a usable SNR. Alternatively, sensitivity can be expressed as the detector's response per unit radiation exposure, such as the output signal (e.g., current, voltage, or charge) generated per unit dose or incident photon energy. High sensitivity implies the detector can resolve weak radiation signals or operate effectively at lower doses. So, the sensitivity can be defined as:

$$S = \frac{I_p - I_d}{DA} \tag{9}$$

where I_p is photocurrent, I_d represents dark current, D represents the radiation dose rate, and A represents the effective detection area of the ionizing radiation photodetector.

4.1.2. Detection Limit

The detection limit of an ionizing radiation detector refers to the lowest radiation dose rate that the detector can reliably distinguish from its intrinsic noise with a specified confidence level (usually, the signal-to-noise ratio ≥ 3). It represents the practical threshold below which the detector cannot conclusively determine whether a signal originates from radiation or random noise fluctuations.

4.1.3. Mobility-Lifetime Product ($\mu\tau$)

The mobility-lifetime product is a critical material parameter for semiconductor-based ionizing radiation detectors. It quantifies the efficiency of charge carrier transport within the detector material by combining two key properties:

1) Mobility (μ): The average drift velocity of charge carriers (electrons or holes) per unit electric field (unit: cm^2/V·s).
2) Lifetime (τ): The mean time a charge carrier survives before being trapped or recombined (unit: seconds).

High $\mu\tau$ values can enable near-complete charge collection, which is essential for high-resolution spectroscopy.

4.1.4. Light Yield (LY) of Scintillator

LY is a critical parameter that quantifies a scintillator's efficiency in converting the energy deposited by ionizing radiation into detectable photons (UV, IR, or visible light). It is defined as the

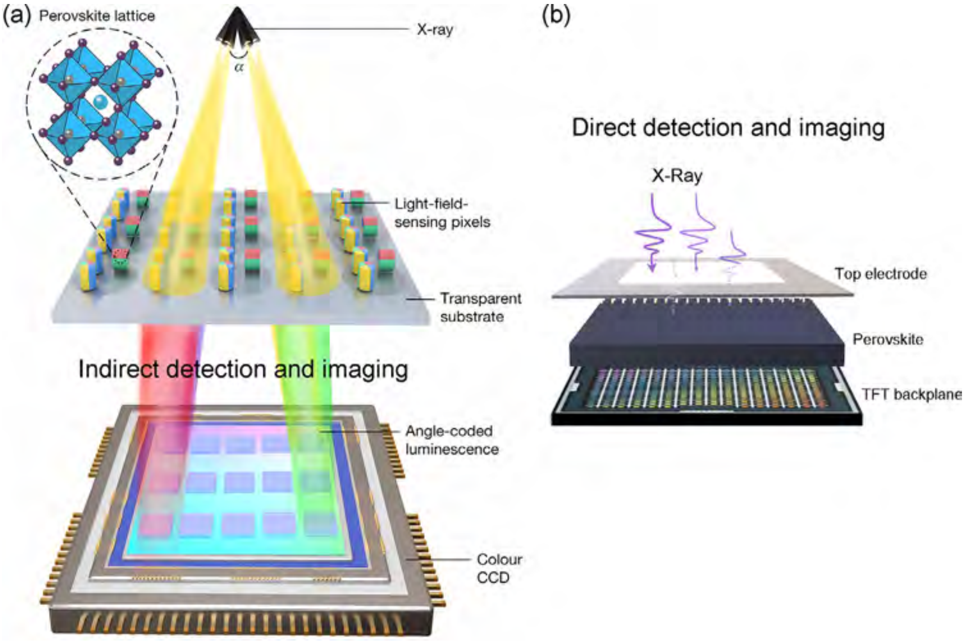

Figure 13. Schematic of the structure of basic radiation detectors. a) The indirect scintillator detector. Light-field-sensing pixels, X-ray into luminescence signals of different colors, can be detected by a color CCD.[89] Copyright 2023, Springer Nature. b) The direct detector. The incident X-ray photons are absorbed by semiconductors, generating tons of electron-hole pairs.[90] Copyright 2024, American Chemical Society.

number of scintillation photons produced per unit of energy deposited by the incident radiation , typically expressed in photons per megaelectronvolt (photons/MeV) . LY can be represented as:

$$LY = \frac{SQ}{\beta E_g} \tag{10}$$

where S represents the quantum efficiency of the transport stage, and Q represents the quantum efficiency of the emission stage, βE_g represents the energy required to generate one electron-hole pair, dependent on the material bandgap (E_g) and an empirical parameter (β, typically 2–3) that accounts for energy conversion inefficiencies.

4.2. X-Ray Detectors

X-ray technology holds transformative potential across critical sectors, including future healthcare systems, advanced industrial processes, and aerospace engineering. The effective utilization of this radiation fundamentally depends on the precise detection and characterization of X-ray signals, serving as a cornerstone for practical applications. This technological imperative drives the need to develop next-generation X-ray detectors that combine exceptional performance metrics with minimized noise characteristics – a critical priority for advancing X-ray-based solutions across scientific and industrial domains.[85–88]

Current X-ray detection technologies employ two distinct operational paradigms. The primary approach utilizes scintillator-mediated indirect conversion, where high-energy X-ray photons undergo wavelength-shifting through phosphor materials to produce lower-energy UV–vis photons, subsequently captured by photodetectors (**Figure 13a**).[89] However, this indirect detection architecture is fundamentally constrained by compromised signal integrity, manifested through three interrelated deficiencies: suboptimal detection sensitivity stemming from multi-stage energy conversion losses, persistent optical crosstalk arising from photon scattering phenomena within the scintillator-photodiode interface, and progressive signal attenuation that ultimately degrades spatial resolution and contrast fidelity in proportion to diminishing conversion efficiencies. Alternatively, direct detection architectures achieve superior signal fidelity through semiconductor-based energy conversion mechanisms, enabling an immediate transformation of incident X-ray photons into measurable electrical signals within the detector medium itself (Figure 13b).[90] Nonetheless, X-ray direct detectors based on α-Se and CdTe exhibit several critical limitations, including prohibitively high production costs and limited detection sensitivity.

In recent years, halide perovskites have proven promising for X-ray detection.[91] Perovskite materials demonstrate dual-domain technological significance, extending beyond their well-documented photovoltaic capabilities to establish new benchmarks in radiation detection. HPLSCs particularly distinguish themselves from polycrystalline thin-film variants because of their reduced grain boundary density, enabling carrier transport optimization, precise thickness tunability through advanced crystallization control, and enhanced material packing density approaching theoretical maxima, etc. Significantly, the elemental composition of lead halide perovskites—incorporating high atomic number (Z) constituents such as I^- (Z = 53), Cs^+ (Z = 55), and Pb^{2+} (Z = 82) —confers exceptional radiation attenuation coefficients. This fundamental material property renders them particularly suitable for high-energy photon detection scenarios.

4.2.1. Indirect X-Ray Detectors

Halide perovskite scintillators are promising for next-generation indirect X-ray detection because of their superior optoelectronic performance characterized by exceptional photoluminescence quantum yield (PLQY) and expansive color gamut coverage. Especially for HPLSCs, the low-defect nature endows them with even higher luminescence efficiency, making them more promising for next-generation indirect X-ray detectors.

$Cs_3Cu_2I_5$ scintillator has recently emerged as a research hotspot. As a lead-free perovskite derivative, $Cs_3Cu_2I_5$ exhibits high light yield, ultrafast scintillation decay time, and excellent energy resolution. Tang et al. reported one Mg^{2+}-doped $Cs_3Cu_2I_5$ HPLSC (**Figure 14a**), achieving a record PLQY of 81.7%. Low-temperature PL studies revealed Mg-related defect states near the self-trapped exciton (STE) energy levels. These states provided additional carrier capture pathways, enhancing STE emission and reducing nonradiative losses, a novel mechanism for optimizing copper-based halide scintillators (Figure 14b). Then, a hydrophobic $Cs_3Cu_2I_5$:Mg@PMMA flexible indirect X-ray detector was fabricated, achieving a spatial resolution of 2.5 lp mm^{-1} under low-dose X-ray irradiation (200 μGy) (Figure 14c). This resolution meets commercial spiral CT requirements and surpasses many lead-based perovskite films. This work demonstrated Mg^{2+} doping to simultaneously enhance PLQY, light output, and structural and radiation stability in copper-based halide scintillators.[92]

Dong et al. introduced $HCOO^-$ doping at the halide sites of $Cs_3Cu_2I_5$ crystals, which is a novel and environmentally friendly approach to modulate emission properties without toxic elements. The halide perovskite scintillator achieved multiexciton emissions induced by $HCOO^-$-triggered lattice distortion (Figure 14d). The doped $Cs_3Cu_2I_5$ crystals demonstrated an obvious improvement in light yield (61 500 photons MeV^{-1}, which is 5.4 times larger than that of the pristine $Cs_3Cu_2I_5$, Figure 14e), surpassing commercial CsI:Tl scintillators (≈54 000 photons MeV^{-1}). This work pioneered a non-toxic doping strategy to unlock multiexciton emissions in copper halide perovskite scintillator.[93]

Some other novel lead-free HPLSC scintillators have also been proposed. Gong et al. developed hybrid manganese HPLSCs, $(Br\text{-}PrTPP)_2MnBr_4$ (Br-PrTPP = (3-bromopropyl) triphenylphosphonium) and $(Br\text{-}BuTPP)_2MnBr_4$ (BrBuTPP = (4-bromobutyl) triphenylphosphonium). These materials demonstrate outstanding RL performance, with a light yield of 68 000 photons MeV^{-1}, surpassing commercial NaI:Tl (54 000 photons MeV^{-1}) and outperforming most reported manganese-based scintillators. The $(Br\text{-}PrTPP)_2MnBr_4$ crystal-based X-ray indirect detector achieved a detection limit of 45 nGy_{air} s^{-1}, which is 122 times lower than the medical diagnostic requirement (5.5 μGy_{air} s^{-1}) and superior to lead-free alternatives like $Cs_2AgBiBr_6$ (59.7 nGy_{air} s^{-1}) (Figure 14f). Besides, a flexible scintillator film fabricated from $(Br\text{-}PrTPP)_2MnBr_4$ and PDMS achieves an ultrahigh spatial resolution of 12.78 lp mm^{-1}, exceeding commercial CsI:Tl (10 lp mm^{-1}) (Figure 14g,h). This work pioneers a new class of environmentally friendly, high-performance scintillators for X-ray detection and imaging technologies.[94]

Li et al. introduced a novel zirconium-based perovskite scintillator, $(C_8H_{20}N)_2ZrCl_6$, as a non-toxic alternative to traditional lead-based perovskites. The synthesized HPLSCs achieve a remarkably high photoluminescence quantum yield (PLQY) of 80.77%, surpassing previous zirconium-based perovskites (e.g., Cs_2ZrCl_6 with ≈70% PLQY) (Figure 14i). This is attributed to the large organic cation $C_8H_{20}N^+$, which isolates $ZrCl_6$ octahedra and enhances electron wavefunction localization, minimizing self-absorption. They then integrated $(C_8H_{20}N)_2ZrCl_6$ into a PDMS matrix, creating flexible, large-area (5 cm×5 cm) composite films (Figure 14j). The $(C_8H_{20}N)_2ZrCl_6$@PDMS scintillator achieved a spatial resolution of 5.8 lp mm^{-1}.[95]

Doping strategies have also been proven effective in enhancing the scintillation performance of HPLSCs. Wang et al. reported one scintillator, Rb_2AgBr_3:Cu. They doped Cu into Rb_2AgBr_3 for the first time using the TLC method. The Rb_2AgBr_3:Cu single crystal achieves a high light yield, outperforming commercial benchmarks like GAGG:Ce and CsI:Na (Figure 14k). They also achieved flexible and stable scintillator films by mixing Rb_2AgBr_3:Cu single crystals with PDMS. The Rb_2AgBr_3:Cu@PDMS films enabled high-resolution X-ray imaging of non-planar objects with 10.2 lp mm^{-1} spatial resolution. The scintillator films exhibited exceptional stability under continuous X-ray irradiation (0.5 h) and humid conditions (72% RH for 4 weeks), addressing deliquescence issues in conventional halide scintillators. The excellent performance of the Rb_2AgBr_3:Cu single crystals is derived from the following mechanism: controlled Cu^+ doping promotes bromine vacancy formation, which acts as a trapping center for excitons, significantly boosting light yield and photoluminescence quantum yield.[96]

4.2.2. Direct X-Ray Detectors

Benefiting from the high atomic numbers of the constituent elements, centimeter-scale thickness, and high crystallinity of HPLSCs, they hold greater potential for direct X-ray detection.

Tao et al. developed a novel Ar-HBr mixed atmosphere edge-defined film-fed growth (EFG) technique to grow high-quality $CsPbBr_3$ HPLSCs (**Figure 15a**). Compared with the conventional VB method, the HPLSCs synthesized by this EFG method had suppressed defects and reduced ion migration (Figure 15b). The corresponding X-ray detector demonstrated an ultrahigh sensitivity of 46 180 μC Gy_{air}^{-1} cm^{-2} at 5000 V cm^{-1} for 120 keV X-rays, surpassing most perovskite-based detectors (Figure 15c). This EFG method enables fast growth rates and large-area crystals for high-performance direct X-ray detection, offering a low-cost, industrially viable solution.[97]

Exploring novel perovskite materials presents a critical pathway to overcome the existing bottlenecks in X-ray detection technologies. Niu et al. reported a novel anti-perovskite material, $(2\text{-}Habch)_3Cl(PtI_6)$ with indirect bandgap transitions and low orbital symmetry at the band edge (the crystal structure is shown in Figure 15d). This design minimizes electron-hole wavefunction overlap, leading to ultralong carrier lifetimes (>3 ms), surpassing traditional perovskites by orders of magnitude (Figure 15e). The single crystal-based X-ray detector demonstrated a detection limit of 2.4 nGy_{air} s^{-1}, which was much lower than medical diagnostic standards and commercial α-Se detectors (Figure 15f). The sensitivity was up to 10^4 μC Gy_{air}^{-1} cm^{-2}, outperforming state-of-the-art perovskite detectors and commercial CdZnTe. Figure 15g

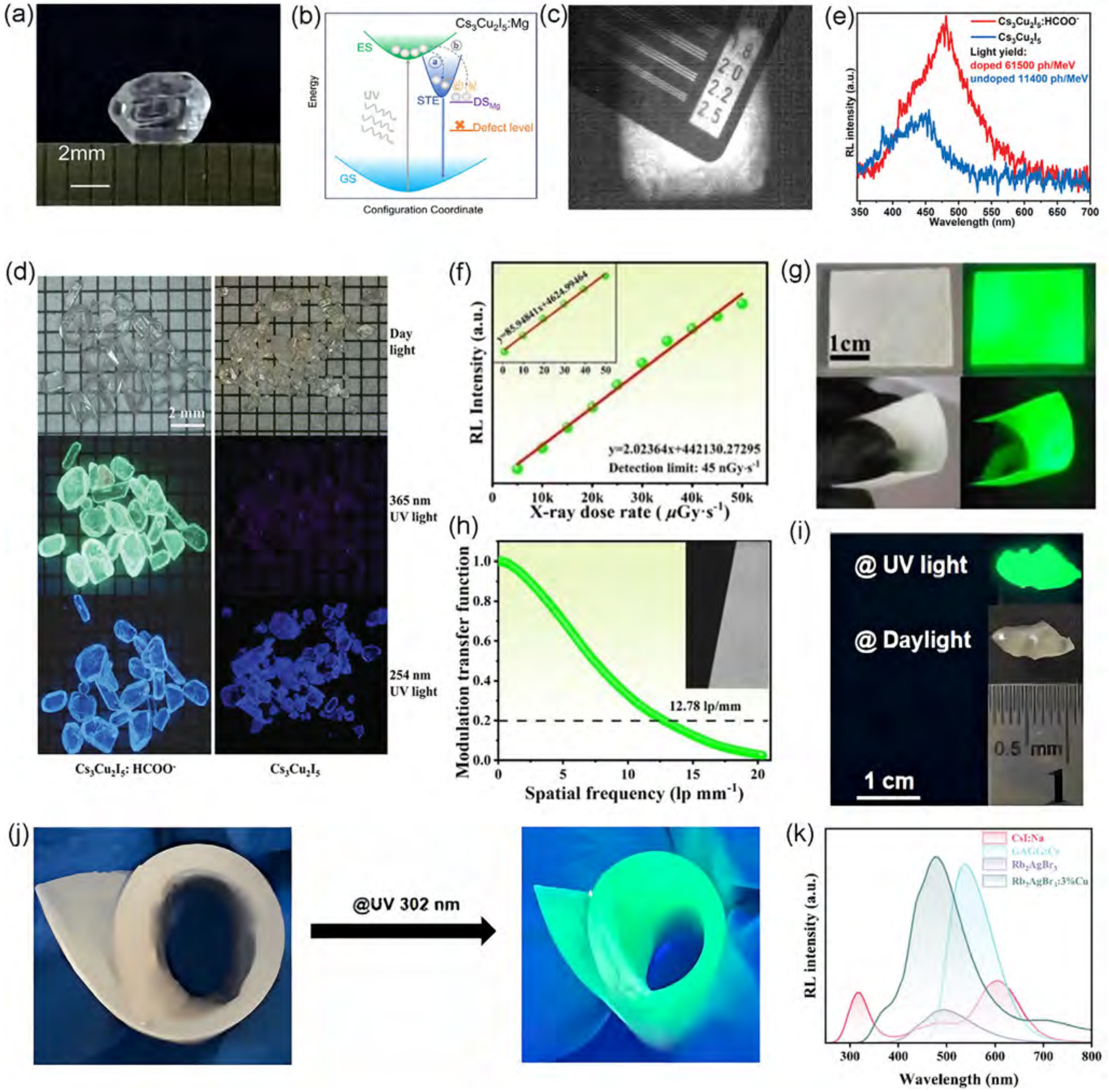

Figure 14. a) Photograph of the as-grown $Cs_3Cu_2I_5$:Mg HPLSCs. b) Proposed STE emission mechanism of $Cs_3Cu_2I_5$:Mg. c) X-ray image of the line-pair card based on the $Cs_3Cu_2I_5$:Mg HPLSC@PMMA flexible film.[92] Copyright 2025, American Chemical Society. d) Images of $Cs_3Cu_2I_5$:$HCOO^-$ and $Cs_3Cu_2I_5$ HPLSCs under sunlight, 365-nm-UV, and 254-nm-UV irradiation. e) Radioluminescence (RL) spectra of pristine and HCOO-doped $Cs_3Cu_2I_5$ HPLSCs.[93] Copyright 2024, John Wiley and Sons. f) Integrated scintillation intensity as a linear function of the X-ray dose rate of $(Br\text{-}PrTPP)_2MnBr_4$. g) Photos of the $(Br\text{-}PrTPP)_2MnBr_4$-based flexible film under daylight and X-ray irradiation at a dose rate of 35 mGyair s^{-1}. h) Modulation transfer function curve of the crystalline scintillation screen.[94] Copyright 2024, American Chemical Society. i) Photograph of $(C_8H_{20}N)_2ZrCl_6$ HPLSC under 302 nm UV light excitation and daylight. j) Photographs of the cylinder of $(C_8H_{20}N)_2ZrCl_6$@PDMS films under white and UV light illumination.[95] Copyright 2025, AIP Publishing. k) RL spectra of Rb_2AgBr_3, Rb_2AgBr_3:Cu, CsI:Na, and GAGG:Ce (voltage: 50 kV, current: 1000 μA).[96] Copyright 2025, Elsevier.

shows the images of the $(2\text{-Habch})_3Cl(PtI_6)$ X-ray detector with dose rates of 93 nGy_{air} s^{-1}.[98]

Designing and constructing perovskite single-crystal heterojunctions can also help to enhance the performance of direct X-ray detectors. Zhang et al. employed a novel liquid-phase epitaxial method with TLC method to achieve high-quality $Cs_2AgBiBr_6/Cs_3Bi_2Br_9$ single-crystalline heterojunction (Figure 15h,i). The structure of the configured X-ray detector is shown in Figure 15j. The heterojunction detector demonstrated a sensitivity of 1390 μC Gy_{air}^{-1} cm^{-2} at room temperature and

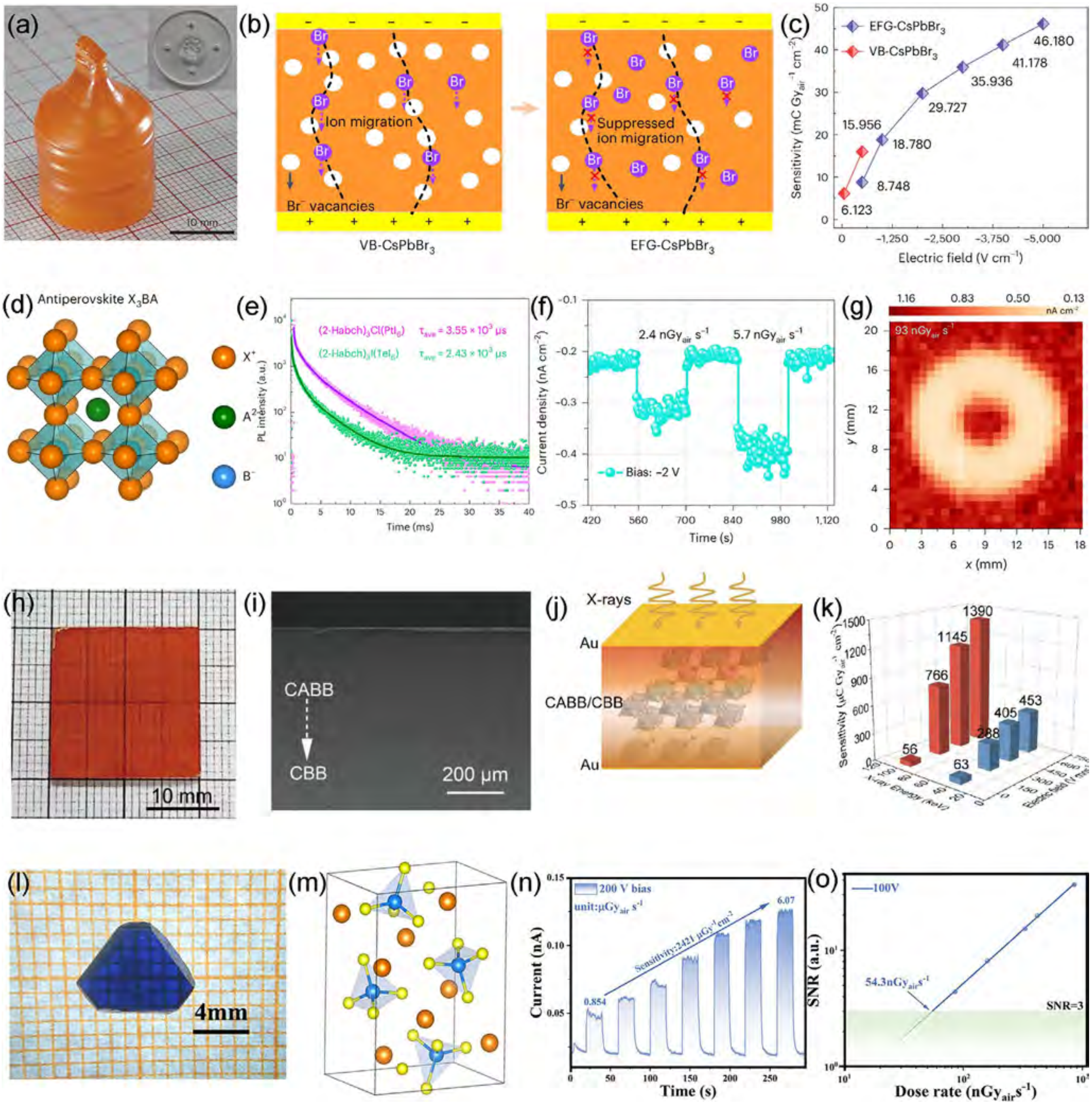

Figure 15. a) Cylindrical CsPbBr$_3$ HPLSC grown from a circular quartz die via the EFG method. b) Schematic of suppressed ion migration through control of the growth atmosphere. c) Sensitivities of EFG- and vertical Bridgman (VB)-CsPbBr$_3$ HPLSC X-ray detectors for 120-keV hard X-rays.[97] Copyright 2024, Springer Nature. d) Simplified crystal structure for the anti-perovskite. e) Time-dependent PL spectra of (2-Habch)$_3$Cl(PtI$_6$) and (2-Habch)$_3$I(TeI$_6$) single crystals. f) The *I-t* curve under weak radiation dose rates of the (2-Habch)$_3$Cl(PtI$_6$) X-ray detector. g) Metal ring images taken by the (2-Habch)$_3$Cl(PtI$_6$) X-ray detector with dose rates of 93 nGy$_{air}$ s^{-1}.[98] Copyright 2024, Springer Nature. h) Photographs of Cs$_2$AgBiBr$_6$/Cs$_3$Bi$_2$Br$_9$ heterostructure HPLSC. i) SEM image of cross-section morphologies of the Cs$_2$AgBiBr$_6$/Cs$_3$Bi$_2$Br$_9$ heterojunction. j) Structure of the HPLSC heterojunction X-ray detector. k) Sensitivities of the heterojunction detector for 40- and 100-keV X-rays under different electric fields.[99] Copyright 2024, Springer Nature. l) Photographic image of a Cs$_2$CoCl$_4$ HPLSC. m) The crystal structure of Cs$_2$CoCl$_4$. n) *I-t* curves of the Cs$_2$CoCl$_4$ HPLSC X-ray detector under increased X-ray dose rates at 200 V bias. o) SNR of Cs$_2$CoCl$_4$ HPLSC X-ray detector under various X-ray dose rates at 100 V bias, giving a LoD of 54.3 nGy$_{air}$ s^{-1}.[100] Copyright 2025, Elsevier.

Table 3. Performance of HPLSC-Based Direct X-ray Detectors.

HPLSC	Growth method	$\mu\tau$ [cm^2 V^{-1}]	Sensitivity [µC Gy$_{\text{air}}$$^{-1}$ cm^{-2}]	Detection Limit [nGy$_{\text{air}}$ s^{-1}]	Refs.
$FPEA_2PbI_4$-$FPEA_2SnI_4$	TLC	4.00×10^{-5}	1.7×10^5	4.2	[101]
$(HIS)_2AgSbBr_8$	TLC	1.72×10^{-3}	223	84.2	[102]
$MAGeI_3$	TLC	1.90×10^{-2}	42 825	4.1	[103]
$(PEA)_2Ge_{0.5}Pb_{0.5}I_4$	TLC	3.64×10^{-3}	13 488	8.23	[104]
$MhyPbBr_3$	TLC	1.10×10^{-3}	220	203	[105]
$MHy_3Bi_2I_9$	TLC	6.26×10^{-4}	106	55	[106]
$GA_3Bi_2Br_9$	TLC	1.13×10^{-3}	1645.7	0.85	[107]
$(Benzylamine)_2CsPb_2Br_7$	TLC	1.50×10^{-5}	1186	16	[108]
$(DFBZA)_2PbCl_4$	TLC	3.94×10^{-4}	293	/	[109]
$(DPDA)PbBr_4$	TLC	6.70×10^{-4}	45.9	13	[110]
$MA_3Bi_2I_6Br_3$	ITC	9.80×10^{-3}	24 509	4.3	[111]
$Cs_{0.1}FA_{0.85}GA_{0.05}Pb(I_{0.9}Br_{0.1})_3$:Sr	ITC	1.29×10^{-2}	2.6×10^4	7.09	[112]
$Cs_3Bi_2I_3Br_6$	Bridgman	1.08×10^{-4}	1516	6.2	[113]
$CsPbBr_3$	Bridgman	2.05×10^{-3}	474	/	[114]

2075 µC Gy$_{\text{air}}$$^{-1}$ cm^{-2} at 75 °C for 100 keV X-rays, outperforming most lead-free perovskite detectors (Figure 15k). The heterojunction exhibited a high ion activation energy (696.5 meV) and low trap density (2.27×10^{10} cm^{-3}), ensuring stable dark current and high X-ray detection sensitivity.[99]

Some new HPLSCs have also been engineered for X-ray detection. Wu et al. synthesized a Cs_2CoCl_4 HPLSC (Figure 15l), one 0D lead-free perovskite. The 0D structure features isolated $[CoCl_4]^{2-}$ tetrahedra separated by large Cs^+ cations, which suppressed ion migration and enhanced structural stability (the crystal structure is shown in Figure 15m). The Cs_2CoCl_4 single-crystal X-ray detector achieved a sensitivity of 2421 µC·Gy$_{\text{air}}$$^{-1}$·cm^{-2} at 287.8 V·mm^{-1}, surpassing organic–inorganic hybrid perovskites (e.g., $(BA)_2PbI_4$) and commercial inorganic semiconductors (Figure 15n). A detection limit of 54.3 nGy$_{\text{air}}$·s^{-1} (SNR = 3) was also achieved, which is 100× lower than the medical diagnostic threshold (5.5 µGy$_{\text{air}}$.s^{-1}) (Figure 15o). DFT calculations revealed that charge transport in Cs_2CoCl_4 is dominated by $[CoCl_4]^{2-}$ tetrahedra, with minimal contribution from Cs^+ ions. This explains the material's high resistivity and suppressed ion migration. This work demonstrated the application of 0D lead-free HPLSCs in direct X-ray detection, offering a sustainable alternative to toxic lead-based perovskites and traditional semiconductors.[100]

Table 3 summarizes the key performance parameters for state-of-the-art HPLSC-based direct X-ray detectors reported recently.

4.3. γ-Ray Detectors

γ-ray detection plays pivotal roles across multidisciplinary sectors, including medical diagnostics (CT/PET imaging, radiotherapy monitoring), astrophysical observations (space telescope payloads), nuclear facility safety protocols, and contraband screening systems.[119–121] HPLSCs have recently emerged as disruptive candidates for next-generation γ-ray detectors.

Kanatzidis et al. revealed that $CsPbBr_xCl_{3-x}$ perovskites crystallize in a monoclinic phase (space group $P2_1/m$) at room temperature, overturning prior assumptions of an orthorhombic (Pnma) symmetry. This monoclinic structure features a fourfold larger unit cell volume and a $\sqrt{2}\times\sqrt{2}$ superstructure, resolving inconsistencies in earlier diffraction studies. The Br/Cl alloying suppressed the number of phase transitions from two to one across most compositions, minimizing lattice strain, twin domain formation, and defects during crystal growth (**Figure 16a**). The Bridgman-grown $CsPbBr_2Cl$ HPLSC (Figure 16b) based γ-ray detector achieved an energy resolution of 7.2% for ^{57}Co γ-ray (122 keV) at 200 V bias, rivaling commercial detectors like CZT while offering lower production costs (Figure 16c). This work redefines the structural understanding of $CsPbBr_3Cl_{3-x}$ perovskites, enabling defect-suppressed HPLSC growth, establishing a pathway for perovskite-based radiation detectors.[115]

High-quality HPLSCs have been proven to be indispensable for high-performance γ-ray detectors. Huang et al. developed a novel solvent system combining DMF, GBL, and DMSO to balance the solubility slopes of $CsPbBr_3$ and $FAPbBr_3$. This enabled precise control over the Cs/FA ratio in $FACsPbBr_3$ crystals during growth (Figure 16d). The HPLSCs obtained by this strategy achieved a record-low deep trap density of 5.6×10^{10} cm^{-3}, 20-fold lower than pure $CsPbBr_3$. The $FACsPbBr_3$ HPLSC γ-ray detectors achieved an energy resolution of 2.9% at 662 keV (^{137}Cs γ-rays), rivaling high-end CZT detectors (Figure 16e). Key metrics included high resistivity (9.5×10^9 Ω·cm), balanced mobility-lifetime products ($\mu\tau$: 3.2×10^{-3} cm^2 V^{-1} for holes, 2.2×10^{-3} cm^2 V^{-1} for electrons), and 84% charge collection efficiency, enabling precise detection of γ-rays across 59.5–662 keV. This work's mixed-solvent strategy and defect-suppression mechanisms effectively optimized other hybrid perovskite systems toward γ-ray detection.[116]

Surface states were also demonstrated to be important γ-ray detectors. Yuan et al. synthesized high-quality $MAPbBr_3$ HPLSCs via the ITC method (Figure 16f). They then introduced a strong electron-withdrawing ligand, 4-trifluoromethyl-benzylamine, which induced minimized defect density and interfacial charge displacement at the $MAPbBr_3$ HPLSCs surface,

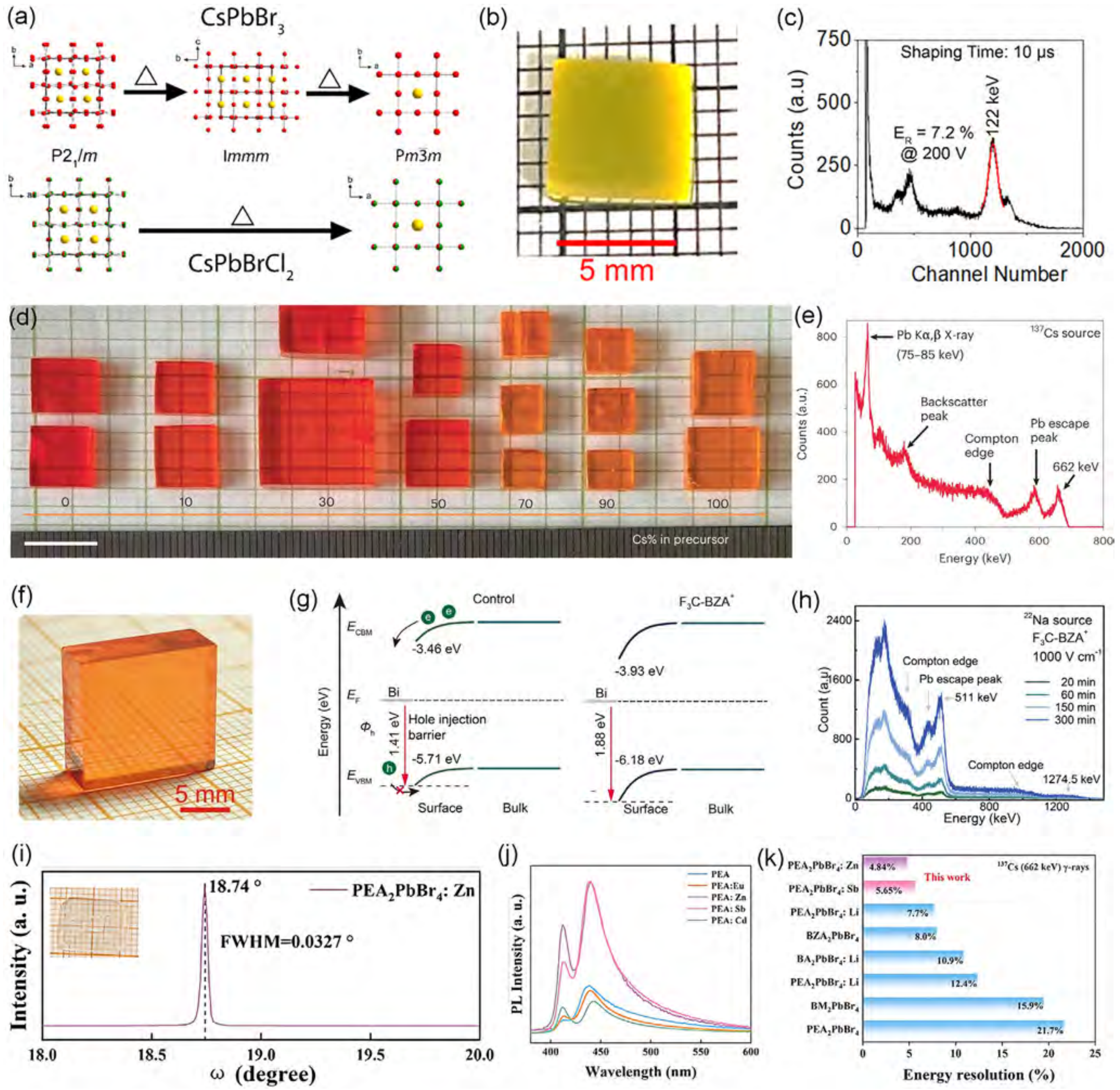

Figure 16. a) The depiction of the phase transition pathway for $CsPbBr_3$ and $CsPbBrCl_2$, highlighting the reduction of phase transitions with halide mixing. b) $CsPbBr_2Cl$ HPLSC prepared for γ-ray detector fabrication. c) The ^{57}Co γ-ray spectrum at 200 V with the energy resolution calculated.[115] Copyright 2024, American Chemical Society. (d) A photograph of several as-grown $FA_xCs_{1-x}PbBr_3$ HPLSCs from different precursor solutions with Cs/(Cs + FA) ratios varying from 0% to 100%. Scale bar, 1 cm. e) Energy-resolved spectrum of a ^{137}Cs γ-ray source with a 662 keV photopeak and a shaping time of 1 μs.[116] Copyright 2023, Springer Nature. f) Photograph of the control $MAPbBr_3$ HPLSC. g) Schematic of the band bending at the perovskite surface after contact equilibrium with the metal electrode. h) Operation stability measurement of control and F_3C-BZA^+-treated detectors under ^{22}Na γ-ray source.[117] Copyright 2024, John Wiley and Sons. i) Photograph of large-sized PEA_2PbBr_4: Zn HPLSCs and XRD rocking curve. j) Photoluminescence spectra of the HPLSCs before and after interstitial doping. k) Comparison of energy resolution under ^{137}Cs with other organic–inorganic 2D perovskite scintillators.[118] Copyright 2025, John Wiley and Sons.

significantly raising the hole injection barrier (from 1.41 to 1.88 eV) and suppressing leakage currents (Figure 16g). The corresponding γ-Ray detectors achieved a record energy resolution of 3.9% for 511 keV γ-rays (^{22}Na source) at room temperature, among the best for perovskite detectors. These detectors maintained stable energy resolution for over 300 min, the longest reported operational longevity for perovskite γ-ray detectors (Figure 16h). These innovations address critical challenges in perovskite γ-ray detection, such as leakage current suppression, defect management, and long-term stability, paving the way for practical applications in medical imaging, security screening, and radiation monitoring.[117]

Doping strategy can also be used to improve the performance of γ-ray detectors. Gao et al. introduced a novel interstitial doping approach using Zn^{2+} and Sb^{3+} cations in PEA_2PbBr_4 HPLSCs. The interstitial doping induces lattice expansion, reduces defects, and suppresses exciton-exciton annihilation, minimizing non-radiative losses (Figure 16i). This strategy significantly enhances crystallinity and optical performance (Figure 16j). The Zn^{2+}- and Sb^{3+}-doped scintillators achieve unprecedented energy resolutions of 4.84% and 5.65% at 662 keV γ-rays, surpassing previous reports for 2D organic–inorganic perovskite scintillators (Figure 16k). This work positions Zn/Sb-doped PEA_2PbBr_4 as a cost-effective, multifunctional alternative to conventional scintillators like $LaBr_3$ and stilbene derivatives.[118]

5. Stability Engineering for HPLSC Photodetectors

Despite significant advances in HPLSC photodetectors, stability remains the primary obstacle to commercialization.[122,123] Halide perovskites exhibit inherently weak ionic bonds, making them vulnerable to degradation under light, moisture, and oxygen. Low activation energies for ion migration also cause phase segregation (e.g., Hoke effect) and defect accumulation.[124] Therefore, improving the stability of perovskite photoelectric devices remains a persistent challenge. In this section, we will analyze recent progress in the stability research of HPLSC photodetectors.

5.1. Storage Stability

Storage stability is crucial for perovskite photoelectric devices to be used long-term. As mentioned above, H_2O molecules can rapidly penetrate the perovskite lattice, causing decomposition. To cope with the problem, hydrophobic long-chain organic layers are introduced into traditional 3D perovskites, leading to the fabrication of quasi-2D perovskites (including DJ, RP, and alternating cations intercalation (ACI) phases). The DJ and ACI phases exhibit significantly superior stability to the RP phase.[125] First, stronger hydrogen bonding replaces RP's van der Waals gaps in DJ and ACI phases, creating rigid barriers against ion migration.[126] Second, ACI phases incorporate MA^+ cations to suppress dielectric confinement, reducing exciton binding energy (to 50–100 meV, near 3D perovskites vs 200–300 meV in RP). This mitigates self-trapped exciton (STE)-induced lattice strain and non-radiative heat accumulation, enabling devices like $(GA)(MA)_2Pb_2I_7$ to retain 85.5% photocurrent after 1000s operation.[81] Third, the DJ and ACI phases achieve exceptional lattice rigidity via minimal octahedral distortion, enhancing thermal/environmental resilience.[127] So, dimensional engineering is an effective approach to improving HPLSC stability.

Inspired by the dimensional engineering, Luo et al. for the first time achieved a mixed low-dimensional structure (1D-0D) in an Ag-Bi HPLSC, $(4\text{-AP})_5AgBi_3Br_{20}$ (4-AP = 4-amidinopyridine), which showed impressive storage stability, thermal stability, and operation stability (**Figure 17a**). The 1D chains provide efficient carrier transport pathways; meanwhile, the 0D isolated units suppress ion migration due to their discrete nature. So, the 1D-0D combination balances structural integrity and charge transport. The corresponding X-ray detector still exhibited excellent performance after 70 days of storage, with only a slight decrease in photoresponse (Figure 17b).[128]

Besides, Debroye et al. found that doping lead-free $Cs_2AgBiBr_6$ HPLSCs with noble metal cations (Au^{3+}, Pd^{2+}, Ir^{3+}) could also preserve and leverage the intrinsic stability. The doped HPLSCs exhibited excellent long-term stability under ambient conditions. PXRD patterns recorded after storing the doped crystals for 6 months in air showed no significant changes in their crystalline structure compared to freshly synthesized samples (Figure 17c).[129] The work highlights that functional enhancement by noble metal cations doping can be achieved without sacrificing the core stability advantages of this lead-free perovskite class.

Surface engineering strategy has also proven effective in enhancing the stability of HPLSCs. Zhou et al. employed a dual-step solvent-based surface treatment to $MAPbBr_3$ HPLSCs with 1-Octadecene and EMIMBr ionic liquid, respectively. They found that the 1-octadecene step prevents the formation of surface cavities caused by redissolution during crystal removal/cooling, resulting in a smoother surface (as shown by AFM, Figure 17d). The $EMIMPbBr_3$ capping layer provided structural integrity to the surface, which made the crystal surface more resistant to moisture damage (Figure 17e). The corresponding photodetectors exhibited dramatically improved long-term stability.[130] This work introduced a simple, solvent-based surface treatment method to improve the stability of the HPLSCs.

5.2. Irradiation Stability

Irradiation can create or modify the material's electrically active defects (trap states). These traps capture charge carriers, reducing conductivity and detector sensitivity, which will even accumulate over time, causing permanent damage.[133,134] Conventional 3D perovskites can easily undergo reversible chemical decomposition under radiation.

Cavalcoli et al. investigated the radiation-induced instability in PEA_2PbBr_4 HPLSCs (synthesized by the SEE method). They revealed the PEA_2PbBr_4 HPLSCs' exceptional radiation hardness compared to conventional 3D perovskites. The superior stability of the PEA_2PbBr_4 HPLSCs was derived from their suppressed ion migration, enhanced structural integrity, and self-healing nature. The X-ray detectors retained full functionality after 200 Gy of X-ray radiation. This stability is crucial for applications like X-ray detectors, where ionizing radiation typically degrades performance.[135]

Jin et al. also reported the DJ type $BDA_2AgBiBr_8$ HPLSC (synthesized by AVC method)-based X-ray detector with record sensitivity and ultrahigh stability. The unencapsulated $BDA_2AgBiBr_8$ detectors could withstand $> 1000\ Gy_{air}$ cumulative dose with $<$ 7% degradation, exceeding medical standards (Figure 17f). This good irradiation stability came from the strong H-bonding of the DJ-type perovskite and the high defect formation energy for Ag/Br vacancies. This work gave an effective way to design high-performance, stable HPLSC-based X-ray detectors.[131]

Fang et al. introduced a rapid, non-thermal IR healing strategy to repair the damage of $MAPbI_3$ HPLSCs (synthesized by the

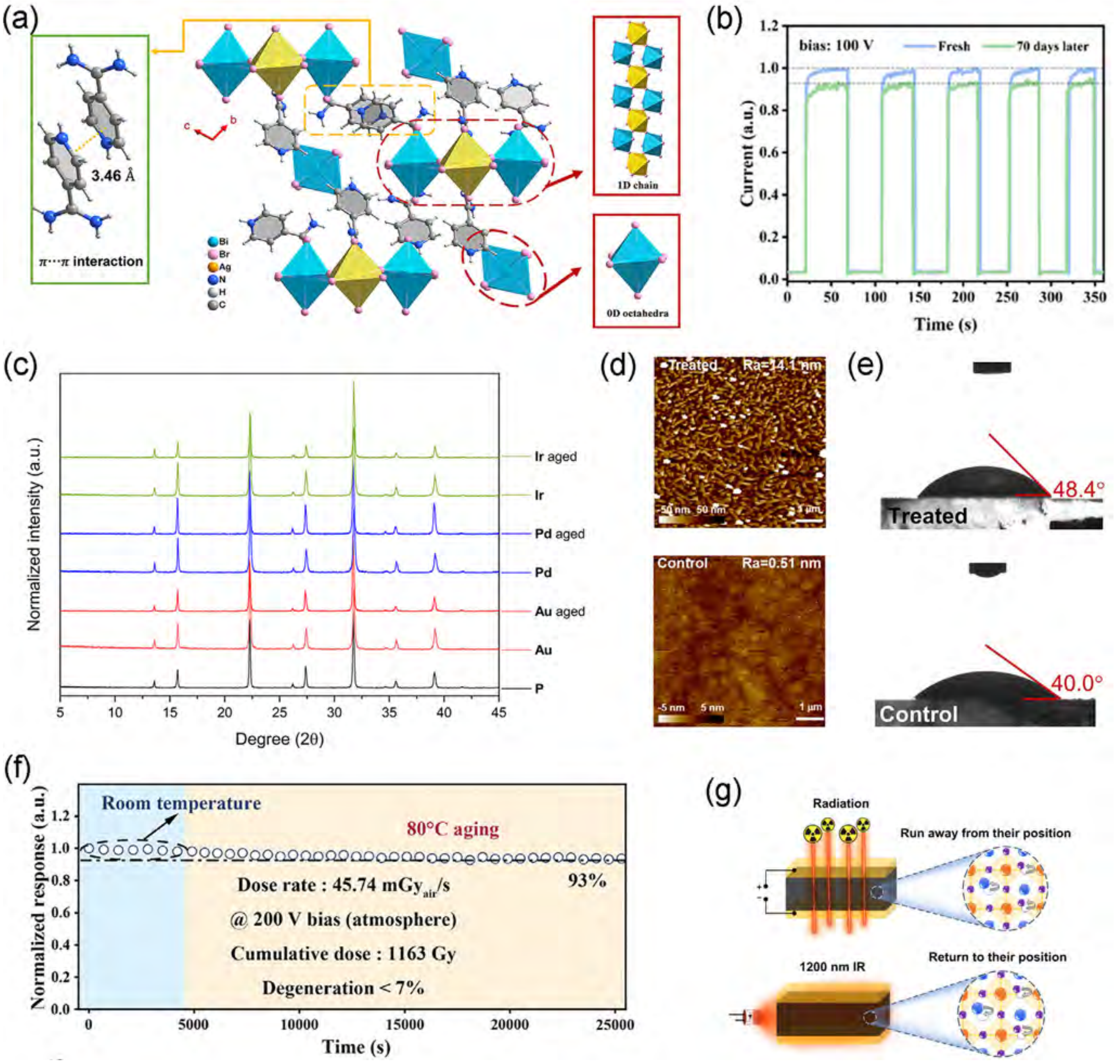

Figure 17. a) Structural diagram of (4-AP)$_5$AgBi$_3$Br$_{20}$. b) The X-ray irradiation response measured after 70 days under a high dose rate of 1989 μGy s^{-1} at 100 V bias.[128] Copyright 2025, John Wiley and Sons. c) PXRD patterns of the pristine and doped materials, both freshly prepared and after six months of storage under ambient conditions.[129] Copyright 2025, John Wiley and Sons. Surface AFM images d) and water contact angle measurements e) of MAPbBr$_3$ HPLSCs with and without surface engineering treatment.[130] Copyright 2025, John Wiley and Sons. f) Operational stability of BDA$_2$AgBiBr$_8$ HPLSC X-ray detector under continuous X-ray irradiation and 80 °C high temperature.[131] Copyright 2023, John Wiley and Sons. g) The schematic illustration of the ion migration with bias, radiation, and under infrared illumination.[132] Copyright 2024, American Chemical Society.

ITC method) from radiation. They exposed the corresponding degraded device to 1200 nm IR light (10 mW cm^{-2}) for 1 h. The IR penetrated deep into crystals without heating, which lowered its ion-migration activation energy and decreased the defect density (Figure 17g). This IR healing method rapidly repaired irradiation-induced defects in perovskite detectors, a viable strategy to enhance device longevity in high-radiation environments.[132]

Some other HPLSCs can even self-heal after the radiation damage. Alresheedi et al. found that the Cs$_3$Bi$_2$I$_9$ HPLSCs (synthesized by the TSSG method) exhibited remarkable structural and compositional stability under light irradiation. Their unique electronic response involved a reversible, light-triggered conductivity (NPC) decrease caused by metastable trap states. These metastable trap states were induced by the radiation of visible light. The light-induced degradation could be impressively followed by a slow self-recovery in the dark. This behavior is distinct from permanent material degradation.[134]

5.3. Stability Issues of Lead-Free HPLSCs

While lead-based perovskites demonstrate remarkable performance, their inherent toxicity is an insurmountable obstacle for large-scale, sustainable, and ethically responsible commercialization.[136] Developing efficient, stable, and truly lead-free perovskite materials is essential. However, lead-free perovskites are plagued by even more stability issues.[137] This section analyzes the stability problems in lead-free perovskites and reviews recent advances in addressing these issues.

Sn-based HPLSCs are promising due to their superior optoelectronic properties, which have a narrow bandgap (1.15–1.3 eV), extended carrier diffusion lengths, and high absorption coefficients ($>10^4$ cm^{-1}), ideal for efficient light harvesting.[138,139] However, Sn-based HPLSCs face serious stability challenges: Sn^{2+} can easily be oxidized to Sn^{4+} in air, causing rapid degradation; there are also tin vacancy defects in these materials, where the intrinsic Sn vacancies act as acceptors, increasing hole concentration and non-radiative recombination.[140,141]

Many efforts have been made to solve the stability problem of Sn-based HPLSCs. Wei et al. reported a strategy using oxalic acid as a reductant in the TLC method to grow high-quality $FPEA_2SnI_4$ HPLSCs under ambient conditions. This addressed the critical problem of Sn^{2+} oxidation during crystal growth, which traditionally required inert atmospheres or complex acid solutions (like HI with H_3PO_2) and led to poor crystal quality and high defect density. The oxalic acid approach significantly improves crystal quality and stability, and reduces defects. Furthermore, to protect the tin perovskite surface after growth in devices, the authors constructed a single-crystal heterojunction by growing a bandgap-matched lead perovskite ($FPEA_2SnI_4$) layer on top of the tin perovskite. This heterojunction X-ray detector achieved a high sensitivity of 1.7×10^5 μC Gy^{-1} cm^{-2}.[101]

Sn^{4+}-based HPLSCs have also been proposed, which could avoid the drawback of Sn^{2+} oxidation. Vijayakumar et al. developed a novel 0D Sn^{4+}-based halide perovskite, $(AEHB)_2SnBr_6$ (AEHB: N-(2-aminoethyl)-2-hydroxybenzamide). The $(AEHB)_2SnBr_6$ HPLSCs were synthesized using the TLC method. This material exhibited anisotropic photoconductivity and an exceptionally long charge carrier lifetime. These properties endowed the corresponding deep-UV photodetector with outstanding performance, with a high responsivity of 9.96 A W^{-1} and high detectivity of 6.8×10^{11}. Thanks to the robust Sn^{4+}, the photodetector also had long-term stability (4 weeks).[77]

Unlike the Sn^{2+} based HPLSCs, the Bi^{3+} and Sb^{3+} based ones have much more enhanced stability against oxidation. However, they also face other stability issues. For example, their A-site cations, traditional amine-based organic cations (MA^+, FA^+, Gua^+), have N—H bonds, forming strong hydrogen bonds with external H_2O molecules. This makes the perovskite hygroscopic and susceptible to moisture-induced degradation. To address this issue, Tang et al. synthesized a novel lead-free bismuth HPLSC, $(C_9H_{14}N)_3Bi_2I_9$ (where $C_9H_{14}N^+$ is the phenyltrimethylammonium cation. The $C_9H_{14}N^+$ cation is fully alkylated, eliminating hydrogen bond donors, dramatically improving the moisture stability by preventing the primary hydrolysis pathway initiated by H-bonding with water. Besides, this bulky cation also induced significant structural distortions and tilting of the $[Bi_2I_9]^{3-}$ units, reducing the interlayer spacing. The reduced interlayer spacing was proven to improve the operational stability of the detectors under bias.[142] Apart from the A site cations induced instability, the Bi^{3+} and Sb^{3+} based perovskites also suffer phase change at different temperatures, which will cause the lattice distortions, increasing trap density, and reducing light absorption/emission efficiency.[143] So, the Bi^{3+} and Sb^{3+} HPLSCs-based device should be operated above critical temperatures for $Cs_3Bi_2I_9$, maintain $T > -55$ °C to avoid hexagonal-monoclinic transition. Thermal annealing control through precise annealing (e.g., 90 °C for $Cs_3Bi_2I_9$ films) prevents unwanted phase segregation.[144]

6. Summary and Perspective

HPLSCs have become a groundbreaking material platform for photodetection technologies, spanning optical and ionizing radiation regimes. This review captures the swift advancements in HPLSC-based detectors, highlighting their advantages in carrier transport efficiency, spectral tunability, and radiation attenuation. Advanced synthesis techniques like TLC, ITC, AVC, SSE, and Bridgman methods have produced crystals with defect densities as low as 10^8–10^{10} cm^{-3}, carrier mobilities over 10^2 cm^2 V^{-1} s^{-1}, and dimensions from millimeters to centimeters. These attributes support exceptional device performance: visible-light detectors with responsivities above 10^4 AW^{-1}, UV photodetectors with sub-nanosecond response times, and X-ray detectors with sensitivities exceeding 10^4 μC Gy_{air}^{-1} cm^{-2}. The structural versatility of HPLSCs has enabled multifunctional detection paradigms, with low-dimensional perovskites extending spectral coverage to deep-UV and NIR regions, and heterojunction designs facilitating self-powered operation. Innovations in defect engineering have improved stability and detection limits. For ionizing radiation detection, HPLSCs' high atomic number and cm-scale thickness offer superior stopping power, achieving energy resolutions of 2.9% at 662 keV for γ-rays and spatial resolutions of 13.9 lp mm^{-1} for X-ray imaging.

Despite these advancements, challenges remain. Scalability is a major hurdle; while TLC and ITC methods produce high-quality crystals, industrial adoption requires reproducible growth of HPLSCs larger than 10 cm^3 with sub-ppm impurity levels. Environmental stability under operational stresses—moisture, thermal cycling, and prolonged irradiation—needs improvement, especially for lead-based systems. The toxicity of Pb and instability of Sn in narrow-bandgap perovskites call for eco-friendly alternatives, such as Bi, Cu, and Sb-based derivatives or organic–inorganic hybrids with enhanced ligand protection. At the same time, developing novel high-efficiency process methodologies for sustainable Pb recovery merits equal attention. Additionally, fundamental device physics limitations, including inefficient gate-field modulation in bulk phototransistors and polarization-induced signal drift in ferroelectric detectors, demand innovative architectural solutions.

Looking ahead, several strategies could significantly advance the development of HPLSC-based photodetectors:

1) Innovative Crystal Growth: Developing novel synthesis methods to produce HPLSCs with superior quality and larger dimensions. Hybrid techniques could merge the scalability of solution processes with the precision of melt growth, aiming

for wafer-sized HPLSCs with uniform optoelectronic properties.

2) Enhanced Stability: Improving the stability of HPLSCs by integrating hydrophobic encapsulation layers and redox-inert dopants to reduce ion migration and oxidation, extending operational lifetimes under demanding conditions.
3) Lead-Free Alternatives: Advancing eco-friendly Pb-free perovskite materials using machine learning-guided high-throughput compositional screening. Focus on Cu/Ag/Bi-based heterostructures that exhibit intrinsic defect tolerance and high effective atomic numbers for superior X-ray photon interaction.
4) Device Physics Optimization: Designing refined device architectures through advanced structural engineering, such as asymmetric electrode configurations, interfacial dipole engineering, and photonic crystal integration, to improve charge extraction efficiency while reducing dark currents.
5) Monolithic System Integration: Developing protocols for wafer-scale fabrication of HPLSC-based photodetector arrays that can be directly integrated with CMOS readout circuits. Techniques like in situ crystallization patterning could enable multifunctional modules for imaging, spectroscopy, and neural interfaces.

The convergence of these efforts could facilitate the transition of HPLSC technology from laboratory breakthroughs to industrial standardization. Interdisciplinary collaboration and connecting materials science, device engineering, and systems integration will be crucial. With ongoing innovation, HPLSCs have the potential to elevate photodetector technology significantly.

Acknowledgements

The authors acknowledge the Hunan Provincial Natural Science Foundation of China (Grant No. 2025JJ60403), Shenzhen Municipality Science and Technology Innovation Commission (Project No. JCYJ20230807114910021), Guangdong Basic and Applied Basic Research Fund (Project No. 2024A1515011922), and the City University of Hong Kong (Project Nos. 7006109, 7020088, and 9229138).

Conflict of Interest

The authors declare no conflict of interest.

Keywords

halide perovskite, ionizing radiation detection, photodetector, single crystal

Received: May 16, 2025
Revised: July 30, 2025
Published online: August 26, 2025

---

[1] A. Rogalski, F. Wang, J. Wang, P. Martyniuk, W. Hu, *Small Methods* **2024**, *9*, 2400709.
[2] Z. Li, T. Yan, X. Fang, *Nat. Rev. Mater.* **2023**, *8*, 587.
[3] F. Wang, T. Zhang, R. Xie, Z. Wang, W. Hu, *Nat. Commun.* **2023**, *14*, 2224.
[4] B. Wei, B. Zou, J. Liu, W. Wang, W. Wang, Z. Cao, T. Han, F. Li, W. Luo, L. Shan, M. Long, *Adv. Funct. Mater.* **2024**, *34*, 2315194.
[5] N. M. Nguyen, D. A. Ngo, L. N. Nguyen, H. N. Luong, H. N. Duy Huynh, B. G. Man Nguyen, N. G. Doan, L. T. Duy, A. V. Tran, C. K. Tran, K. N. Pham, V. Q. Dang, *RSC Adv.* **2023**, *13*, 21703.
[6] Y. Wei, W. Zhang, C. Hou, Q. Zhang, Y. Li, H. Wang, *Sci. China Mater.* **2021**, *64*, 1770.
[7] M. Ghasemi, J. Lu, B. Jia, X. Wen, *Chem. Soc. Rev.* **2025**, *54*, 1644.
[8] N. Pai, D. Angmo, *Adv. Sci.* **2025**, *12*, 2412666.
[9] W. Shao, J. H. Kim, J. Simon, Z. Nian, S.-D. Baek, Y. Lu, C. B. Fruhling, H. Yang, K. Wang, J. Y. Park, L. Huang, Y. Yu, A. Boltasseva, B. M. Savoie, V. M. Shalaev, L. Dou, *Science* **2024**, *384*, 1000.
[10] Z. Xing, G. Jin, Q. Du, P. Pang, T. Liu, Y. Shen, D. Zhang, B. Yu, Y. Liang, D. Yang, J. Tang, L. Wang, G. Xing, J. Chen, D. Ma, *Adv. Mater.* **2024**, *36*, 2406706.
[11] S.-C. Feng, Y. Shen, X.-M. Hu, Z.-H. Su, K. Zhang, B.-F. Wang, L.-X. Cao, F.-M. Xie, H.-Z. Li, X. Gao, J.-X. Tang, Y.-Q. Li, *Adv. Mater.* **2024**, *36*, 2406706.
[12] *National Renewable Energy Laboratory. (n.d.). Best research-cell efficiency chart*, https://www.nrel.gov/pv/interactive-cell-efficiency.html (accessed: July 2025).
[13] S. Li, Y. Jiang, J. Xu, D. Wang, Z. Ding, T. Zhu, B. Chen, Y. Yang, M. Wei, R. Guo, Y. Hou, Y. Chen, C. Sun, K. Wei, S. M. H. Qaid, H. Lu, H. Tan, D. Di, J. Chen, M. Grätzel, E. H. Sargent, M. Yuan, *Nature* **2024**, *635*, 82.
[14] X. Li, S. Aftab, M. Mukhtar, F. Kabir, M. F. Khan, H. H. Hegazy, E. Akman, *Nano-Micro Lett.* **2024**, *17*, 28.
[15] W.-H. Gao, C. Chen, *Nano Energy* **2024**, *128*, 109904.
[16] W. Yang, Y. Lei, Z. Jin, *J. Mater. Chem. C* **2024**, *12*, 7497.
[17] X. Zhou, Z. Lu, L. Zhang, Q. Ke, *Nano Energy* **2023**, *117*, 108908.
[18] W. Li, M. Li, Y. He, J. Song, K. Guo, W. Pan, H. Wei, *Adv. Mater.* **2024**, *36*, 2309588.
[19] D. Fu, Y. Ma, S. Wu, L. Pan, Q. Wang, R. Zhao, X.-M. Zhang, J. Luo, *InfoMat* **2024**, *6*, 12602.
[20] S. Chen, Y. Zhang, J. Zhao, Z. Mi, J. Zhang, J. Cao, J. Feng, G. Zhang, J. Qi, J. Li, P. Gao, *Sci. Bull.* **2020**, *65*, 1643.
[21] Q. Luo, D. Xie, Y. Tian, C. Zhang, D. Cao, X. Chen, P. Liang, H. Shu, *J. Mater. Chem. C* **2024**, *12*, 13061.
[22] Y.-T. Chen, Z.-X. Wen, C.-F. Lin, M.-H. Li, P. Chen, *NPG Asia Mater.* **2024**, *16*, 34.
[23] X. Li, X. Du, P. Zhang, Y. Hua, L. Liu, G. Niu, G. Zhang, J. Tang, X. Tao, *Sci. China Mater.* **2021**, *64*, 1427.
[24] H. Tsai, F. Liu, S. Shrestha, K. Fernando, S. Tretiak, B. Scott, D. T. Vo, J. Strzalka, W. Nie, *Sci. Adv.* **2020**, *6*, aay0815.
[25] Y. Lin, Y. Bai, Y. Fang, Q. Wang, Y. Deng, J. Huang, *ACS Energy Lett.* **2017**, *2*, 1571.
[26] M. Girolami, F. Matteocci, S. Pettinato, V. Serpente, E. Bolli, B. Paci, A. Generosi, S. Salvatori, A. Di Carlo, D. M. Trucchi, *Nano-Micro Lett.* **2024**, *16*, 182.
[27] J. Liu, X. Li, J. Zhao, H. Liu, T. Lin, *J. Alloys Compd.* **2025**, 1021.
[28] G. Zheng, H. Wu, S. He, H. Li, Z. Dong, T. Jin, J. Pang, R. Masrour, Z. Zheng, G. Niu, L. Xu, J. Tang, *Small* **2024**, *21*, 2408720.
[29] N. Liu, D. Chu, X. Xin, J. Tian, Y. Jiang, N. Liang, B. Jia, Y. Liu, S. Liu, *Adv. Funct. Mater.* **2025**, 2504203.
[30] Y. Song, Z. Duan, L. Peng, J. Zhang, X. Zhu, Q. Feng, Z. Ji, Y. Zou, J. Zhang, Z. Li, Z. Zhang, X.-L. Zhang, F. Xie, H. Zhang, Q. Jin, *ACS Nano* **2025**, *19*, 3312.
[31] C. Shen, D. Sun, Y. Dang, K. Wu, T. Xu, R. Hou, H. Chen, J. Wang, D. Wang, *Inorg. Chem.* **2022**, *61*, 16936.
[32] Y. Wang, Q. Guan, Z.-K. Zhu, H. Ye, H. Li, Y. Zeng, P. Yu, H. Yang, W. Wu, J. Luo, *Chem. Sci.* **2025**, *16*, 5283.
[33] M. Daoudy, N. Gouitaa, F. Z. Ahjyaje, L. T-e, F. Abdi, *J. Mater. Res.* **2024**, *39*, 1411.
[34] Y. Li, H. Shen, Y. Li, Y. Gu, J. Zhao, L. Li, J. Xu, *Ceram. Int.* **2024**, *50*, 32603.

[35] J. Li, Y. Yang, Z. Ye, D. Chen, J. Cui, Q. Huang, Y. Zhu, G. Zhang, T. Men, Y. Zuo, J. Zheng, L. Zhao, C. Zhou, Z. Liu, B. Cheng, *J. Mater. Sci. Technol.* **2025**, *232*, 276.
[36] M. Nur-E-Alam, M. A. Islam, Y. B. Kar, T. S. Kiong, H. Misran, M. U. Khandaker, Y. Fouad, M. E. M. Soudagar, E. Cuce, *Sci. Rep.* **2024**, *14*, 19995.
[37] A. D. Valueva, S. A. Novikov, J. Bledsoe, Y. Cai, A. A. Maksimova, J. Locklin, Y. Zhao, V. V. Klepov, *MRS Commun.* **2024**, *14*, 942.
[38] X. Jia, H. Jiang, X. Chong, W. Ju, T. Feng, Z. Zhao, H. Wei, J. Li, S. Cheng, J. Wang, *J. Mater. Chem. C* **2025**, *13*, 2844.
[39] J. Zhang, Y. Yang, W. Li, Z. Tang, Z. Hu, H. Wei, J. Zhang, B. Yang, *Sci. Adv.* **2024**, *10*, ado0873.
[40] H. Yin, M. Liao, Y. Shi, Z. Liu, H. Li, S. He, Z. Zheng, L. Xu, J. Tang, G. Niu, *Adv. Mater.* **2025**, *37*, 2415957.
[41] Y. Haruta, H. Ye, P. Huber, N. Sandor, A. Pavesic Junior, S. Dayneko, S. Qiu, V. Yeddu, M. I. Saidaminov, *Nat. Synth.* **2024**, *3*, 1212.
[42] V. Anilkumar, A. Mahapatra, J. Nawrocki, R. D. Chavan, P. Yadav, D. Prochowicz, *Adv. Opt. Mater.* **2023**, *12*, 2415957.
[43] S. Bimli, V. Manjunath, S. R. Mulani, A. Miglani, R. J. Choudhary, P. A. Shaikh, O. S. Game, R. S. Devan, *ACS Appl. Electron. Mater.* **2024**, *6*, 9091.
[44] S. Han, S. Zhu, G. Fan, X. Huang, G. Zhao, R. Shi, Y. Huang, M. Wu, J. Li, Y. Guo, Y. Gao, S. Zhuang, F. Cao, X. Yu, D. Zhang, *Adv. Funct. Mater.* **2024**, *35*, 2421770.
[45] T. Wang, S. Xin, Y. Liu, Z. Ji, G. Liu, S. Zhang, T. Wang, F. Wang, B. Teng, S. Ji, *J. Mater. Chem. C* **2024**, *12*, 5934.
[46] M. Liao, Z. Wang, C. Shan, D. Luo, Z. Guan, Q. Wang, H. Zhu, Z. Song, D. Wu, A. K. K. Kyaw, K. Wang, *Nano Res.* **2025**, *18*, 94907046.
[47] L. Cong, M. Tan, H. Cui, J. Chen, X. Wang, X. Chu, C. Wu, H. Zhou, *Laser Photonics Rev.* **2025**, e02213.
[48] H. Zhou, M. Tan, Y. Wang, X. Wang, J. Chen, X. Wang, X. Chu, L. Cong, *Opt. Express* **2024**, *32*, 45348.
[49] X. Zhou, Z. Lu, L. Zhang, Q. Ke, *Nano Energy* **2023**, *117*, 108908.
[50] D. Li, W. Xu, D. Zhou, Y. Ji, N. Ding, X. Chen, J. Zhu, R. Sun, S. Lu, C. Ma, Z. Jia, G. Qin, X. Bai, H. Song, *Adv. Opt. Mater.* **2021**, *9*, 2100423.
[51] L. Lu, W. Weng, Y. Ma, Y. Liu, S. Han, X. Liu, H. Xu, W. Lin, Z. Sun, J. Luo, *Angew. Chem., Int. Ed.* **2022**, *61*, 202205030.
[52] C.-X. Li, S.-B. Cho, S.-H. Sohn, I.-K. Park, *J. Alloys Compd.* **2024**, *973*, 172925.
[53] J. Ma, M. Zhang, H. Jiang, X. Chen, Di Wu, X. Li, Y. Zhang, C. Shan, Z. Shi, *Nano Today* **2023**, *52*, 101970.
[54] J. Ma, X. Xia, S. Yan, Y. Li, W. Liang, J. Yan, X. Chen, D. Wu, X. Li, Z. Shi, *ACS Appl. Mater. Interfaces* **2021**, *13*, 15409.
[55] J. Zhao, X. Wang, Y. Pan, Y. Xu, Y. Li, J. Chen, J. Wu, Q. Li, Z. Zhao, X. Zhang, J. Akram, B. S. Bae, H. Yang, W. Lei, *Front. Phys.* **2021**, *9*.
[56] D. Sudarsan, R. Ganguly, A. L. Koner, S. K. Batabyal, *Adv. Mater. Technol.* **2025**, *10*, 2401573.
[57] W. Wang, S. Xu, Z. Lai, X. Feng, H. Qi, Q. Pan, Z. Yang, J. Kang, Y. Li, X. Shu, Z. Zhang, Y. Zhu, J. Bai, F. Hong, J. Qin, R. Xu, Y. He, F. Xu, L. Wang, *Inorg. Chem. Front.* **2024**, *11*, 589.
[58] J. Bai, H. Wang, J. Ma, Y. Zhao, H. Lu, Y. Zhang, S. Gull, T. Qiao, W. Qin, Y. Chen, L. Jiang, G. Long, Y. Wu, *J. Am. Chem. Soc.* **2024**, *146*, 18771.
[59] Z. Cheng, K. Liu, J. Yang, X. Chen, X. Xie, B. Li, Z. Zhang, L. Liu, C. Shan, D. Shen, *ACS Appl. Mater. Interfaces* **2019**, *11*, 34144.
[60] D. Fu, W. Jia, S. Wu, J. Chang, Z. Chen, J. Luo, *Chem. Mater.* **2023**, *35*, 2541.
[61] W. Ahmad, L. Pan, K. Khan, L. Jia, Q. Zhuang, Z. Wang, *Adv. Funct. Mater.* **2023**, *33*, 2300686.
[62] A. Elbanna, H. Jiang, Q. Fu, J.-F. Zhu, Y. Liu, M. Zhao, D. Liu, S. Lai, X. W. Chua, J. Pan, Z. X. Shen, L. Wu, Z. Liu, C.-W. Qiu, J. Teng, *ACS Nano* **2023**, *17*, 4134.
[63] D. Han, J. Wang, L. Agosta, Z. Zang, B. Zhao, L. Kong, H. Lu, I. Mosquera-Lois, V. Carnevali, J. Dong, J. Zhou, H. Ji, L. Pfeifer, S. M. Zakeeruddin, Y. Yang, B. Wu, U. Rothlisberger, X. Yang, M. Grätzel, N. Wang, *Nature* **2023**, *622*, 493.
[64] T. Wang, H.-L. Loi, Q. Cao, G. Feng, Z. Guan, Q. Wei, C. Chen, M. Li, Y. Zhu, C.-S. Lee, F. Yan, *Adv. Mater.* **2024**, *36*, 2402947.
[65] J. Yu, J. Zheng, H. Chen, N. Tian, L. Li, Y. Qu, Y. Huang, Y. Luo, W. Tan, *J. Mater. Chem. C* **2022**, *10*, 274.
[66] Y. Liu, Y. Li, W. Lu, T. Lan, Z. Chen, W. Ning, Y. Wang, B. Sun, *Chem. Eng. J.* **2025**, *508*, 160881.
[67] Y. Ma, L. Shan, Y. Ying, L. Shen, Y. Fu, L. Fei, Y. Lei, N. Yue, W. Zhang, H. Zhang, H. Huang, K. Yao, J. Chu, *Nat. Commun.* **2024**, *15*, 7516.
[68] M. H. Miah, M. U. Khandaker, M. B. Rahman, M. Nur-E-Alam, M. A. Islam, *RSC Adv.* **2024**, *14*, 15876.
[69] B. Yao, H. M. Hamzah, S. F. B. W. M. Hatta, F. Arith, M. Nur-E-Alam, M. A. Islam, *J. Opt.* **2025**, https://doi.org/10.1007/s12596-025-02786-5.
[70] W. Hu, R. Yan, Y. Ma, R. Cong, X. Ning, D. Zhang, D. Zhang, Y. Liu, L. Li, S. Wang, Z. Yang, C. Pan, L. Guo, *Laser Photonics Rev.* **2025**, *19*, 24019090.
[71] W. Wang, Q. Wei, Y. Gong, G. Xing, B. Wu, G. Zhou, *Adv. Opt. Mater.* **2022**, *10*, 2200400.
[72] R. K. Ulaganathan, P. K. Roy, S. M. Mhatre, R. C. Murugesan, W.-L. Chen, M.-H. Lai, A. Subramanian, C.-Y. Lin, Y.-M. Chang, S. Canulescu, A. Rozhin, C.-T. Liang, R. Sankar, *Adv. Funct. Mater.* **2023**, *33*, 2214078.
[73] S. Han, J. Quan, D. Wang, H. Li, X. Liu, J. Xu, Y. Zhang, Z. Li, L. Wu, X. Fang, *Adv. Sci.* **2023**, *10*, 2206417.
[74] Z. Jia, M. P. Davydova, T. S. Sukhikh, H. Liu, Y. Liu, A. V. Artem'ev, Q. Lin, *Adv. Funct. Mater.* **2024**, *35*, 2413612.
[75] Z. Ji, Y. Liu, T. Wang, G. Liu, B. Teng, S. Ji, *Inorg. Chem.* **2024**, *63*, 7422.
[76] K. Liu, Q. Zhang, C. Wang, L. Wang, F. Chen, *Cryst. Growth Des.* **2025**, *25*, 2552.
[77] A. Ajayakumar, C. Muthu, M. G. Basavarajappa, A. V. Dev, R. Nishikubo, S. Chakraborty, A. Saeki, L. Dou, C. Vijayakumar, *Adv. Funct. Mater.* **2023**, *34*, 2304899.
[78] H. Wang, H. Hu, K. Homewood, Y. Gao, *Opt. Mater.* **2024**, *151*, 115327.
[79] C. Wang, W. Cao, H. Shen, H. Gao, H. Zhou, X. Guo, *Eur. J. Inorg. Chem.* **2025**, *28*, 202400628.
[80] C. Zhang, H. Xiao, Q. Guan, T. Zhu, L. Liang, R. Li, H. Ye, X. Niu, J. Luo, *J. Mater. Chem. C* **2023**, *11*, 5116.
[81] Y. Li, Z. Lai, Y. Meng, W. Wang, Y. Zhang, X. Zhao, D. Yin, W. Wang, P. Xie, Q. Quan, S. Yip, J. C. Ho, *J. Materiomics* **2023**, *9*, 817.
[82] J. Liu, W. Nie, L. Yan, H. Hu, G. Zhang, P. Lin, H. Hu, L. Xu, P. Wang, C. Cui, *J. Phys. D: Appl. Phys.* **2024**, *57*, 335101.
[83] D. K. Jarwal, N. Jingar, M. Kulhar, R. Kumar, A. Bera, *Sens. Actuators, A* **2024**, *374*, 115451.
[84] Z. Li, S. Sun, H. Jiang, Z. Ding, C. Zhang, Z. Cui, Y. Wang, Y. Chen, H. Zhong, *Adv. Funct. Mater.* **2024**, *34*, 2407629.
[85] M. C. Folgueras, Y. Jiang, J. Jin, P. Yang, *Nature* **2023**, *621*, 282.
[86] C. Wang, S. Chen, J. Jie, C. Tian, R. Jia, X. Wu, X. Zhang, X. Zhang, *Adv. Funct. Mater.* **2024**, *35*, 2401189.
[87] Y. Wang, Y. Wang, T. A. S. Doherty, S. D. Stranks, F. Gao, D. Yang, *Nat. Rev. Chem.* **2025**, *9*, 261.
[88] H. Zai, P. Yang, J. Su, R. Yin, R. Fan, Y. Wu, X. Zhu, Y. Ma, T. Zhou, W. Zhou, Y. Zhang, Z. Huang, Y. Jiang, N. Li, Y. Bai, C. Zhu, Z. Huang, J. Chang, Q. Chen, Y. Zhang, H. Zhou, *Science* **2025**, *387*, 186.
[89] L. Yi, B. Hou, H. Zhao, X. Liu, *Nature* **2023**, *618*, 281.
[90] F. Yao, K. Dong, W. Ke, G. Fang, *ACS Nano* **2024**, *18*, 6095.
[91] M. H. Miah, M. U. Khandaker, M. Aminul Islam, M. Nur-E-Alam, H. Osman, M. H. Ullah, *RSC Adv.* **2024**, *14*, 6656.
[92] T. Wu, Y. Shi, X. Zuo, M. Chen, H. Ran, S. Zhao, J. Chen, Y. Tang, *Cryst. Growth Des.* **2025**, *25*, 663.

[93] Z. Wang, L. Wang, J. Xie, Y. Yang, Y. Song, G. Xiao, Y. Fu, L. Zhang, Y. Fang, D. Yang, Q. Dong, *Small* **2024**, *20*, 2309922.
[94] J. Zhang, X. Wang, W.-Q. Wang, X. Deng, C.-Y. Yue, X.-W. Lei, Z. Gong, *Inorg. Chem.* **2024**, *63*, 2647.
[95] Y. Guo, B. Wang, X. Zhang, K. An, Z. Zang, R. Li, *Appl. Phys. Lett.* **2025**, *126*, 081901.
[96] Q. Wu, X. Zhou, W. Gui, L. Yao, Y. Wang, C. L. Wang, *Chem. Eng. J.* **2025**, *507*, 160815.
[97] Y. Hua, G. Zhang, X. Sun, P. Zhang, Y. Hao, Y. Xu, Y. Yang, Q. Lin, X. Li, Z. Zhai, F. Cui, H. Liu, J. Liu, X. Tao, *Nat. Photonics* **2024**, *18*, 870.
[98] L. Liu, S.-Y. Liu, Y. Shi, C.-L. Fang, S. Zhao, H.-Y. Shen, M.-X. Chen, Z.-J. Wang, Y. Ma, Y. Liu, Y. Feng, J. Tang, H.-Y. Ye, G. Niu, *Nat. Photonics* **2024**, *18*, 990.
[99] H. Liu, X. Sun, J. Liu, X. Li, Y. Hua, Z. Yue, J. Song, X. Wang, Y. Yang, Q. Lin, Z. Zhai, X. Tao, G. Zhang, *Sci. China Mater.* **2024**, *68*, 561.
[100] X. Zhang, R. Huang, Z. Zhang, H. Lu, H. Sha, X. Xu, Y. Zheng, X. Huang, S. Wang, S. Wu, *Chem. Eng. J.* **2025**, *504*, 158729.
[101] M. Li, Y. He, X. Feng, W. Qu, W. Wei, B. Yang, H. Wei, *Adv. Mater.* **2023**, *35*, 2307042.
[102] Q. Fan, H. Xu, S. You, Y. Ma, Y. Liu, W. Guo, X. Hu, B. Wang, C. Gao, W. Liu, J. Luo, Z. Sun, *Small* **2023**, *19*, 2301594.
[103] M. Chen, X. Zheng, Y. Li, X. Dong, J. Pi, D. Chu, N. Liu, B. Jia, Y. Liang, X. Zhang, Z. Zhao, J. Hao, L. Zhao, Z. Feng, M. Wei, R. Shi, S. (F.). Liu, Y. Liu, *Adv. Opt. Mater.* **2024**, *12*, 2401028.
[104] Y. Liang, Z. Zhao, J. Hao, Y. Zhang, D. Chu, B. Jia, *Nano Lett.* **2024**, *24*, 8436.
[105] Q. Guan, S. You, Z.-K. Zhu, R. Li, H. Ye, C. Zhang, H. Li, C. Ji, X. Liu, J. Luo, *Angew. Chem., Int. Ed.* **2024**, *63*, 202320180.
[106] R. Li, J. Wu, Z.-K. Zhu, Y. Geng, X. Li, Y. Wang, B. Xu, Z. Lin, J. Luo, *Small Sci.* **2025**, *5*, 2400508.
[107] J. Zhang, W. Guo, H. Xu, Q. Fan, Z. Sun, J. Luo, *Chem. Eur. J.* **2025**, *31*, 202403840.
[108] Y. Zheng, P. Yu, Y. Yao, S. You, Z.-K. Zhu, J. Luo, *Sci. China Chem.* **2025**, *68*, 1317.
[109] X. Zeng, Y. Liu, Y. Chen, Q. Fan, T. Yang, L. Tang, W. Guo, Y. Ma, J. Luo, Z. Sun, *ACS Energy Lett.* **2024**, *9*, 381.
[110] S. Choudhary, J. Ghosh, S. Pathak, S. K. Saini, N. K. Tailor, P. Sellin, S. Bhattacharya, S. Satapathi, *Small* **2025**, *21*, 2409962.
[111] Y. Zhang, J. Hao, Z. Zhao, J. Pi, R. Shi, X. Li, N. Yuan, J. Ding, S. (F.). Liu, Y. Liu, *Adv. Mater.* **2024**, *36*, 2310831.
[112] J. Jiang, M. Xiong, K. Fan, C. Bao, D. Xin, Z. Pan, L. Fei, H. Huang, L. Zhou, K. Yao, X. Zheng, L. Shen, F. Gao, *Nat. Photonics* **2022**, *16*, 575.
[113] S. Tie, X. Lu, G. Tang, W. Tian, P.' Lin, J. Zhu, W. Huang, X. Zheng, *J. Phys. Chem. C* **2025**, *129*, 2260.
[114] J. Pang, H. Wu, H. Li, T. Jin, J. Tang, G. Niu, *Nat. Commun.* **2024**, *15*, 1769.
[115] A. Balvanz, K. S. Bayikadi, Z. Liu, T. S. Ie, J. A. Peters, M. G. Kanatzidis, *J. Am. Chem. Soc.* **2024**, *146*, 31836.
[116] L. Zhao, Y. Zhou, Z. Shi, Z. Ni, M. Wang, Y. Liu, J. Huang, *Nat. Photonics* **2023**, *17*, 315.
[117] Y. Feng, Q. Chen, X. Yan, X. Fu, D. Wang, Z. Ding, S. Li, C. Geng, L. Gao, J. Zhang, F. Yang, S. M. H. Qaid, S. Gao, Y. Jiang, M. Yuan, *Angew. Chem., Int. Ed.* **2024**, *63*, 202412685.
[118] Z. Xiang, J. Chen, T. Huang, F. Shen, X. Chen, J. Wang, Y. Wei, W. Wang, H. Cao, X. Ouyang, J. Gao, *Adv. Mater.* **2025**, *37*, 2414784.
[119] C.-D. Fan, G.-Q. Zeng, H.-W. Deng, L. Yan, J. Yang, C.-H. Hu, S. Qing, Y. Hou, *Nucl. Sci. Techniques* **2024**, *35*, 34.
[120] T. Ferri, A. Caracciolo, G. Borghi, M. Carminati, S. Altieri, N. Protti, C. Fiorini, *IEEE Trans. Nucl. Sci.* **2024**, *71*, 1019.
[121] Y. Liu, H. Sun, D. Xu, D. S. Svinkin, J. Delaunay, N. R. Tanvir, H. Gao, C. Zhang, Y. Chen, X.-F. Wu, B. Zhang, W. Yuan, J. An, G. Bruni, D. D. Frederiks, G. Ghirlanda, J.-W. Hu, A. Li, C.-K. Li, J.-D. Li, D. B. Malesani, L. Piro, G. Raman, R. Ricci, E. Troja, S. D. Vergani, Q.-Y. Wu, J. Yang, B.-B. Zhang, Z.-P. Zhu, et al., *Nat. Astron.* **2025**, *9*, 564.
[122] M. Nur-E-Alam, M. S. Islam, T. Abedin, M. A. Islam, B. K. Yap, T. S. Kiong, N. Das, M. R. Rahman, M. U. Khandaker, *Curr. Opin. Colloid Interface Sci.* **2025**, *76*, 101895.
[123] M.. H. Miah, M.. B. Rahman, M. Nur-E-Alam, M. A. Islam, M. Shahinuzzaman, M.. R. Rahman, M.. H. Ullah, M. U. Khandaker, *RSC Adv.* **2025**, *15*, 628.
[124] M.. H. Miah, M.. B. Rahman, M. Nur-E-Alam, N. Das, N. B. Soin, S. F. W. M. Hatta, M. A. Islam, *ChemNanoMat* **2023**, *9*, 202200471.
[125] S.-M. Lee, M. M. Lian, S.-H. Ahn, D.-J. Yeon, Y. Jang, E. Han, Y. Zhang, J.-H. Sul, J.-H. Yun, *Microstructures* **2025**, *5*, 2025006.
[126] Z. Lai, F. Wang, Y. Meng, X. Bu, X. Kang, Q. Quan, W. Wang, C. Liu, S. Yip, J. C. Ho, *Adv. Opt. Mater.* **2021**, *9*, 2101523.
[127] B. Zhang, T. Zheng, J. You, C. Ma, Y. Liu, L. Zhang, J. Xi, G. Dong, M. Liu, S. (F.). Liu, *Adv. Mater.* **2022**, *35*, 2208875.
[128] W. Wu, G. Chen, Y. Wang, J. Wu, Z. K. Zhu, P. Yu, Y. Zeng, H. P. Xiao, H. Yang, L. Xu, K. Li, Y. Wang, J. Luo, *Laser Photonics Rev.* **2025**, e00276.
[129] D. Valli, R. Vanden Brande, V. Herreman, Q. Li, G. Romolini, J. J.-K. Chen, M. Shameem K M, B. Van Hout, L. Sun, Q. Zhao, B. Pradhan, J. Hofkens, E. Debroye, *Small Sci.* **2025**, *5*, 2500135.
[130] M. Sun, Z. Li, L. Liang, T. Chen, Q. Lou, L. Zhao, J. Wang, X. Xu, B. Zhang, Y. Jin, H. Zhou, *Adv. Mater. Technol.* **2025**, 70050.
[131] H. Chen, Z. Li, S. Wang, G. Peng, W. Lan, H. Wang, Z. Jin, *Adv. Mater.* **2023**, *36*, 2308872.
[132] L. Wang, Y. Song, J. Wang, W. Bi, L. Ding, H. Liu, X. Yang, Y. Wang, S. Yuan, Q. Dong, D. Yang, Y. Fang, *ACS Appl. Mater. Interfaces* **2024**, *16*, 44202.
[133] K. Sakhatskyi, B. Turedi, G. J. Matt, E. Wu, A. Sakhatska, V. Bartosh, M. N. Lintangpradipto, R. Naphade, I. Shorubalko, O. F. Mohammed, S. Yakunin, O. M. Bakr, M. V. Kovalenko, *Nat. Photonics* **2023**, *17*, 510.
[134] M. Ben Bechir, F. Alresheedi, *Opt. Mater.* **2024**, *147*, 114621.
[135] A. Ciavatti, V. Foderà, G. Armaroli, L. Maserati, E. Colantoni, B. Fraboni, D. Cavalcoli, *Adv. Funct. Mater.* **2024**, *34*, 2405291.
[136] M.. H. Miah, M. U. Khandaker, M. Hossen, Noor-E-Ashrafi, I. Jahan, M.. Shahinuzzaman, M. Nur-E-Alam, M. Y. Hanfi, M.. H. Ullah, M. A. Islam, *Mater. Adv.* **2025**, *6*, 2718.
[137] M. H. Miah, N.-E. Ashrafi, M. B. Rahman, M. Nur-E-Alam, M. A. Islam, K. A. Naseer, M. Y. Hanfi, H. Osman, M. U. Khandaker, *Mater. Chem. Phys.* **2024**, *319*, 129377.
[138] B. Wu, Y. Zhou, G. Xing, Q. Xu, H. F. Garces, A. Solanki, T. W. Goh, N. P. Padture, T. C. Sum, *Adv. Funct. Mater.* **2017**, *27*, 1604818.
[139] I. Chung, J.-H. Song, J. Im, J. Androulakis, C. D. Malliakas, H. Li, A. J. Freeman, J. T. Kenney, M. G. Kanatzidis, *J. Am. Chem. Soc.* **2012**, *134*, 8579.
[140] E. Jokar, L. Cai, J. Han, E. J. C. Nacpil, I. Jeon, *Chem. Mater.* **2023**, *35*, 3404.
[141] A. Bhardwaj, D. Marongiu, V. Demontis, A. Simbula, F. Quochi, M. Saba, A. Mura, G. Bongiovanni, *Nanomaterials* **2024**, *14*, 1444.
[142] G. Zheng, B. Song, L. Xu, S. He, J. Pang, H. Li, T. Jin, Y. Shi, Z. Zheng, G. Niu, H. Wu, J. Tang, *ACS Appl. Mater. Interfaces* **2025**, *17*, 32711.
[143] H. Liu, R. Rae, J. Dalzell, G. S. Peters, H. Früchtl, A. P. McKay, D. B. Cordes, A. Kumar, C. A. Kirk, F. D. Morrison, *Inorg. Chem.* **2025**, *64*, 13837.
[144] S. P, S. R. Parne, A. T, *Semicond. Sci. Technol.* **2023**, *38*, 125007.

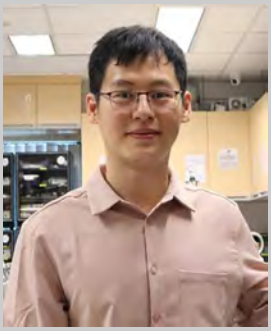

Zhengxun Lai is an Associate Professor at the College of Semiconductors, Hunan University. His research interests focus on halide perovskite-based electronic and photoelectric devices.

Yi Shen is a PhD student at the City University of Hong Kong. His research interests focus on the halide perovskite-based electronic and photoelectric devices.

He Shao is a Post-doctoral Research Fellow in Materials Science and Engineering at the City University of Hong Kong. Her research interests focus on phototransistors, memristors, and synaptic devices.

You Meng is a Professor at the College of Semiconductor (College of Integrated Circuit) at Hunan University. His research interests focus on nanomaterials-based electronics and optoelectronics.

Johnny C. Ho is a Chair Professor of Materials Science and Engineering at the City University of Hong Kong. His research interests focus on the synthesis, characterization, integration, and applications of nanomaterials.